Shape optimization of chilled concrete ceilings – Reduced embodied carbon and enhanced operational performance

Eduardo Gascón Alvarez [*], Natasha L. Stamler, Caitlin T. Mueller, Leslie K. Norford

Massachusetts Institute of Technology, 77 Massachusetts Avenue, Cambridge, MA, 02139, USA

ABSTRACT

The design of lightweight, thermally activated concrete floor systems offers the opportunity to simultaneously tackle two of the most urgent challenges currently faced by the built environment: reducing the use of concrete, responsible for 5–8% of global carbon emissions, and implementing energy-efficient cooling strategies to mitigate the consequences of extreme heat events. This paper introduces a novel chilled concrete ceiling technology integrated into the structural floor slab. This system reduces embodied carbon and enhances operational performance through rigorous structural-thermal shape optimization. As a radiant ceiling with embedded water pipes, the system's cooling capacity improves due to the extended exposed surface provided by the shaping. Additionally, condensation risk decreases as thermal comfort is reached through warmer surface temperatures.

Two cooling-dominated climates and five slab geometries are analyzed using a multi-objective optimization approach, achieving Pareto optimal designs that reduce their embodied carbon by up to 52.5% while achieving 12–14% operational savings relative to conventional prismatic floors. The latter can be reduced by as much as 22–32% at the expense of lowering the embodied savings to 30%. Further, this work introduces a novel method for simulating shaped thermally activated surfaces in Building Energy Modeling (BEM) platforms. An equivalent flat slab model is proposed to transfer the complex 3-D heat transfer processes captured by numerical Conjugate Heat Transfer (CHT) methods into annual, climate-specific simulations. This solution offers a flexible and modular framework that allows architects and engineers to replicate the structural-thermal analysis conducted in this work for other locations and geometries of interest.

1. Introduction

1.1. Integrated building systems for a changing climate

The rapid growth of the urban population worldwide has created an enormous demand for housing that is becoming particularly urgent in many places in the global south. In addition to the evident socioeconomic challenge that this entails, climate change adds yet another layer of complexity. On one hand, the frequency of extreme weather events will increase globally and will likely impact more harshly those regions that, in most cases, have least contributed to Ref. [1]. On the other hand, it is well known that new buildings need to substantially reduce their associated lifespan greenhouse emissions to avoid worsening the consequences of such undesired events. In this context, the research presented here is framed within the broader challenge of developing building systems that simultaneously contribute to climate change mitigation and adaptation. This task must be pursued through a transverse approach that identifies opportunities across disciplines and maximizes the functionalities contained in material shapes and properties. Integration is presented here as an opportunity to increase material efficiency [2] and a path towards a more future-proofed built environment.

1.2. Lightweight, thermally activated floor systems

This paper identifies floor systems in their combined function as spanning structures that carry loads and as exposed surfaces that can be thermally activated through hydronic tubing. Previous work from the authors has demonstrated the possibility of obtaining lightweight, shaped concrete slabs that preserve their thermal mass performance despite a 30% reduction in their structural volume [3]. Here, the main interest lies in the possibility of designing lightweight structural components that minimize their embodied carbon while simultaneously contributing to a low-carbon, resilient cooling strategy. Fig. 1 shows a 1:2 scale

---

prototype conducted to test the technological feasibility of these systems as low-cost, easy-to-implement solutions that can provide buildings with a long-term strategy against extreme heat events. This early-stage shaped concrete slab has been designed following the validated methods proposed in this paper to achieve optimal structural-thermal performance.

2. Previous work

The following sections identify state-of-the-art research within three key fields of work.

2.1. Structural optimization of concrete floor systems

The need for reducing the carbon emissions attributed to concrete is a pressing matter, with cement production accounting for 7–8% of global carbon emissions [4]. Moreover, the building sector floor area is expected to double by 2060 [5], making it necessary to find low-carbon alternatives to conventional concrete frame structures. In response to this enormous challenge, one of the most actionable solutions is to reduce the amount of material needed through structural optimization, ideally concentrating the efforts on those components with the highest savings potential: floor systems [6]. The design of vaulted, unreinforced concrete floor systems by the Block Research Group [7] or the textile-reinforced floors proposed by Hawkins et al. [8] are two clear examples of horizontal structures that achieve significant material savings through an intelligent shaping of the material. The research presented here builds upon the shape optimization methods introduced by Ismail and Mueller for reinforced concrete floor systems that work

structurally in one-way bending [9]; in contrast to other research, this approach is compatible with current building materials and practices in the Global South. This novel 3D parametric framework, described in more detail in Section 3.1, allows for finding the optimal shape for ribbed concrete slabs and achieving up to 64% embodied energy reductions with no loss of strength.

2.2. Shaped radiant cooling systems

In the context of rising global temperatures, radiant cooling systems are increasingly gaining attention as a low-energy, low-carbon approach to achieving thermal comfort. This strategy focuses on the direct cooling of occupants through the radiative heat exchange between the human body and the ceiling surface, allowing the room air to remain at higher room temperatures compared to traditional space-conditioning options. Further, novel research [10] demonstrates the possibility of achieving high ventilation rates with a low impact on the final operational energy, which is particularly relevant in the current context of the COVID-19 pandemic. This work focuses on cooling ceilings that are embedded within construction elements (thermally activated building surfaces, or TABS) and further investigates the potential performance advantages of shaping an activated concrete slab. Within this context, recent research in non-planar ceiling surfaces presents promising improvements in the system's cooling capacity (W/m^2) through, for example, foldable devices (90–100 W/m^2) [11], concave surfaces (70 W/m^2) [12] and inclined fins (77.5 W/m^2) [13]. On a similar note, but applied to thermal mass elements coupled with natural ventilation [14], Fortin and Craig [15] study the geometric activation of building surfaces through rectangular fins or pin arrays.
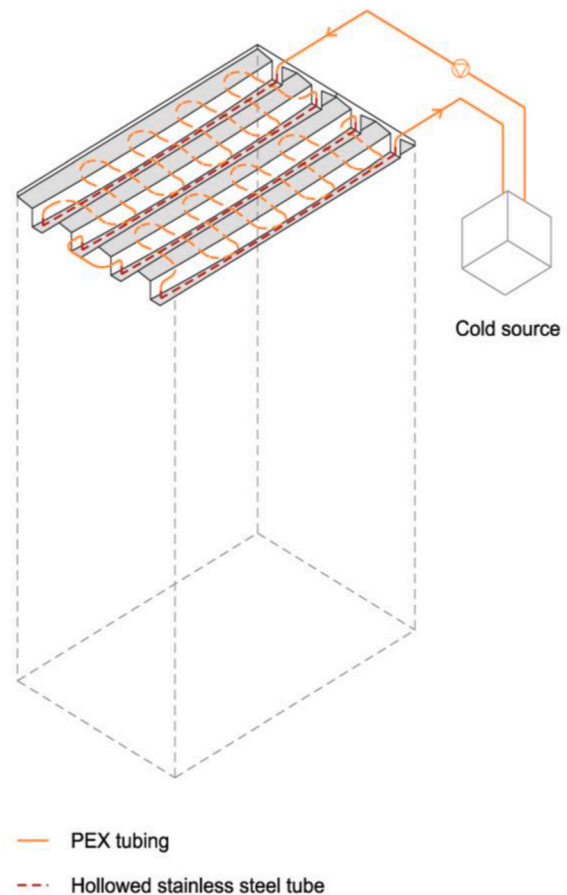
Fig. 1. Construction images of an in-progress technology development test. In an effort towards integration, the stainless-steel tube serves both as structural tensile reinforcement and water channel.

2.3. Integrated simulation frameworks

Among the available literature on radiant systems modeling, this work focuses on integrated simulation frameworks that can simultaneously account for the heat transfer processes within the radiative surface, the interior room environment, and the interface in-between. Early work from Kim et al. [16] showed the potential of fully-coupling Computational Fluid Dynamics (CFD) with a radiative heat transfer simulation and HVAC controlling system. Alternatively, Fonseca et al. proposed a 1-D equivalent thermal network to capture the steady-state behavior of a radiant ceiling panel, which was coupled into a whole-building lumped model that analyzed its dynamic behavior [17]. The method proposed in section 3 combines the advantages of CFD simulations, equivalent thermal networks, and Building Energy Modeling (BEM). More specifically, a technique previously used for studying outdoor heat transfer coefficient in urban neighborhoods is used as a starting point [18]. In that case, Liu et al. use CFD tools to predict the abovementioned coefficients to then extrapolate them as new correlations into a whole-building BEM simulation, providing a flexible and scalable method.

2.4. Research opportunity

Existing literature demonstrates that shaping concrete slabs can benefit both the structural and active thermal performance through an appropriate material distribution, simultaneously reducing the embodied and operational carbon associated with these systems. Open questions center on the applicability and behavior of this building system in specific climates, and methods for identifying and evaluating the best-performing design geometries. In a context of global demand for affordable and low-carbon housing, this paper presents a new application of multi-objective optimization techniques to evaluate comprehensively the design of structurally lightweight, thermally activated concrete floor ceilings for residential use.

3. Method

The presented methodology consists of a modular process that combines analytical and numerical techniques. First, the slabs' structural and thermal performances are simultaneously evaluated through multi-optimization techniques (MOO). This process serves as an analytical approach to finding floor geometries as lightweight and thermally exposed as possible. Then, the preferred designs are analyzed through a set of steady-state conjugate heat transfer simulations to characterize their conductive, convective, and radiative heat transfer processes. This study opens the possibility of implementing an equivalence model that allows modeling the annual performance of shaped cooling ceilings through available whole-building simulation software. Finally, a carbon assessment of the selected geometries is conducted to evaluate their environmental impact from a multi-disciplinary perspective.

3.1. Structural-thermal optimization of concrete slabs

The multi-objective optimization problem presented in this section is defined through the parametrization of the ribbed concrete slab geometry and the definition of the necessary structural-thermal constraints and objectives. The structural analysis is based on recent research on shape optimization [9], minimizing the total embodied carbon of every generated design while ensuring its structural feasibility. Similarly, this paper presents a new metric called the "thermal factor" (TF) to compute the thermal objective. The TF metric is introduced not to give a precise evaluation of the thermal performance but to help the MOO algorithm explore new geometries more efficiently. As explained in this section, this optimization technique requires exploring thousands (tens of thousands in some cases) of design options that otherwise would not be possible to evaluate with more computationally expensive methods.

3.1.1. Variables

The design space is defined by parameterizing the floor's cross-section, following the geometric relations summarized in Fig. 3. Variables a_1 and a_2 establish the width of the slab's ribs at two points and both depend on b, the rib's total amplitude. Variables y_1, y_2 and y_3 determine the depth of the slab at three different heights. This process is repeated in four sections across the floor's length, maintaining b and y_1 constant and allowing the rest of the variables to vary for each case. In total, each design vector x is defined by 18 variables. For this analysis, the final position and size of the steel reinforcement results from the optimization process and are therefore not set as variables.

The design vector x is expressed as follows:

$$x = \begin{bmatrix} a_1 \\ \vdots \\ a_8 \\ y_1 \\ \vdots \\ y_9 \\ b \end{bmatrix} \tag{1}$$

Once the geometric variables are defined, points are interpolated longitudinally across sections. The final geometry is obtained using in-built geometric tools inside Grasshopper3D, a visual programming language commonly used by designers. This same interface incorporates all the other processes included in this section: structural validation, thermal factor calculation, and optimization process.

3.1.2. Constraints and penalty function

Every feasible design must satisfy multiple constraints, most of them governed by the structural behavior of the slabs. Constructability requirements are also incorporated. These constraints, characterized by a set of functions $g(x)$ defined in more detail in Ismail and Mueller's work [9], are the following:

- Ductility requirements: ensure that the ultimate strain for the steel in tension is reached before the concrete's compression failure. This enables the slab to undergo high deflections before collapsing, providing signs of failure.
- Clear cover: checks that the concrete thickness between the rebar and the slab's edge satisfies the building code requirements. This protects the steel from environmental effects that could potentially lead to corrosion.
- Flexural capacity: checks that the bending moment capacity of each analyzed section satisfies the moment envelope at that point.
- Shear capacity: checks that the shear capacity of each analyzed section satisfies the shear envelope at that point.
- Flange thickness: guarantees that the slab's flange is sufficiently stiff to carry the loads from the edges to the central web, across the transverse direction.
- Effective flange width: ensures that the flange is uniformly stressed by checking its width relative to a reference code-defined value.

A penalty function is defined in order to exclude the design options that do not satisfy these constraints, i.e. results outside of the feasible region defined by a total of 18 functions $g_i(x)$. This strategy has been previously applied in similar optimization problems [19]. One of the main challenges is to adequately choose a penalty function that does not modify the feasible results while still helping the algorithm find the Pareto optimal solutions. To achieve that, all constraints are first normalized so that only those designs with values greater than 0 are feasible.
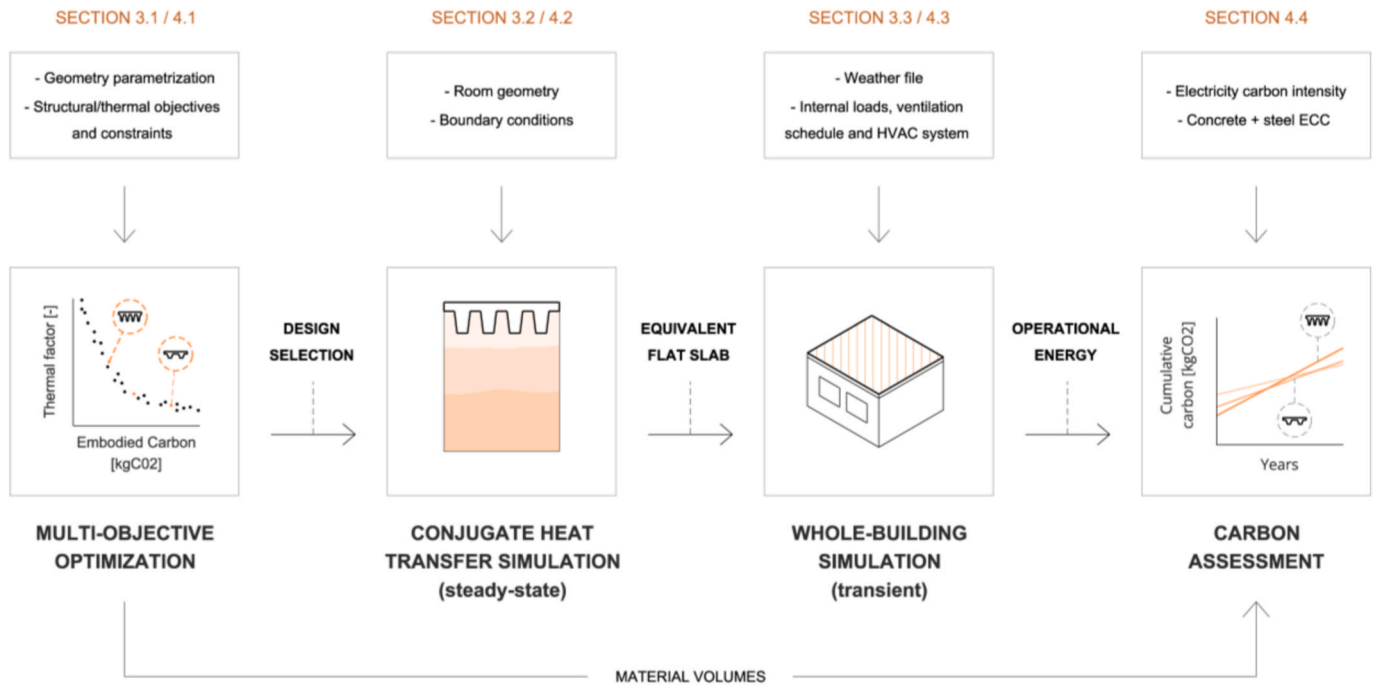
Fig. 2. Multi-step methodology for the design and environmental assessment of lightweight, thermally active concrete slabs. In principle, the same steps could be followed for other shaped TABS. Note: ECC refers to Embodied Carbon Coefficient (kgCO$_{2eq}$/kg).
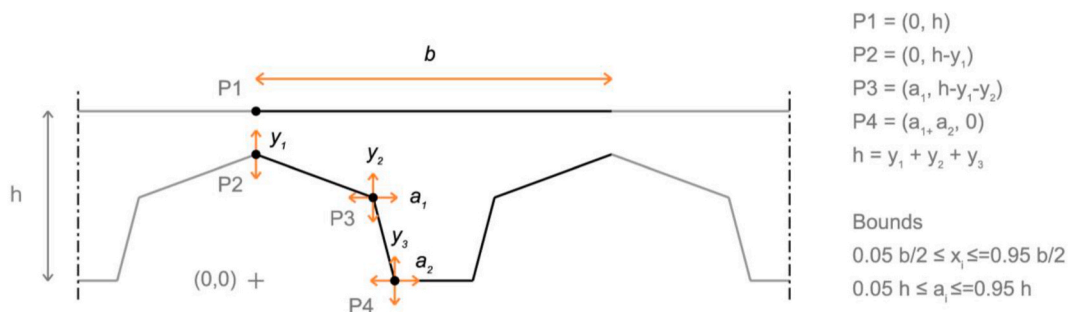
Fig. 3. Slab geometry parametrization through the definition of variables and bounds. Variable 'y$_1$' is kept constant across all four sections, resulting in a total of 9 'y' variable values.

$$g_i(\boldsymbol{x}) \geq 0 \tag{2}$$

Next, a penalty function is applied to these values whenever they are negative, increasing the magnitude of the penalty for more negative – less feasible – values. The penalty function $p_i(g_i(\boldsymbol{x}))$ is defined as:

$$p_i(g_i(\boldsymbol{x})) = \begin{cases} 1 & if \quad g_i(\boldsymbol{x}) \geq 0 \\ (-(g_i(\boldsymbol{x}))^3 + 1 & if \quad g_i(\boldsymbol{x}) < 0 \end{cases} \tag{3}$$

$$P(\boldsymbol{x}) = \frac{\sum_{i=1}^{n} p_i(g_i(x))}{n} \tag{4}$$

The total penalty $P(\boldsymbol{x})$ is computed as the arithmetic mean of all n penalty values obtained from each constraint $g_i(\boldsymbol{x})$ considered. $P(\boldsymbol{x})$ is equal to 1 for fully feasible designs.

3.1.3. Objective functions

The multi-objective optimization process is carried out using the Grasshopper suite *Design Space Exploration* developed by the Digital Structures group [20]. More specifically, the multi-objective optimization tool called MOO, based on the genetic algorithm NSGA-II, is applied [21]. This heuristic method approximates the Pareto front by crossing the higher-performing designs of each generation (the most elite

designs) throughout a given number of iterations. The objective functions $J_1(\boldsymbol{x})$ and $J_2(\boldsymbol{x})$ correspond to the floor's structural and thermal performance, respectively. The former computes the total embodied carbon of both steel and concrete elements using in-built volume calculation functions inside Rhinoceros 3D, the CAD environment used in this work. This function is minimized, understanding that a slab that supports the same loads with less material will structurally behave more efficiently. The second objective corresponds to the thermal factor, which needs to be maximized.

$$J_1(\boldsymbol{x}) = (ECC_{CONCRETE}\,\rho_{CONCRETE}\,V_{CONCRETE}(\boldsymbol{x}) + ECC_{STEEL}\,\rho_{STEEL}\,V_{STEEL}(\boldsymbol{x}))\,P(\boldsymbol{x}) \tag{5}$$

$$J_2(\boldsymbol{x}) = \frac{w_1\,StV(\boldsymbol{x}) + w_2\,F_T(\boldsymbol{x})}{P(\boldsymbol{x})} \tag{6}$$

The definition of this analytical approximation, referred to as "thermal factor," is based on the application of fundamental heat transfer concepts, as well as the study of the CFD simulations used in this work. It is defined by two main geometric characteristics: surface-to-volume ratio *(StV)* and total view factor *(F$_T$)*:

$$Thermal\ factor = w_1\,StV(\boldsymbol{x}) + w_2\,F_T(\boldsymbol{x}) \tag{7}$$

where:

$$StV = \frac{S'}{V} \tag{8}$$

$$F_T = StV \frac{\sum_{i=0}^{n} A_i F_{i-o}}{S'} \tag{9}$$

The surface-to-volume ratio is defined as the ceiling's exposed surface (S') divided by its total volume (V). Geometries with higher StV values will be expected to exchange more energy with the surroundings thanks to their larger exposed surfaces per unit of volume. F_T is the result of multiplying the StV ratio by a weighted average value of all the view factors computed for the different cells in the meshed slab. Each view factor F_{i-o}, which stands between 0 and 1, is obtained by applying the spherical ray intersection methods available in the open-source Ladybug tools [22] for each mesh cell A_i. As explained in more detail in the tool's documentation [45], this component computes the number of rays that do not intersect a given context geometry over the total number of rays projected spherically from the point of interest, giving equal weight to all sphere points. Therefore, geometries that are more exposed to the surroundings (higher F_T) will obtain larger thermal factors than other designs that might have the same StV but present more shadowing between their ribs. Quantities w_1 and w_2 give designers the option of weighting the values of StV and F_T depending on the importance that they decide each metric will play in the final design.

3.2. Numerical modelling of shaped cooling ceilings

The described multi-objective optimization process results in concrete slabs of variable width and depth across their span. A significant part of this geometrical complexity responds to structural priorities, as each analyzed section adapts its shape following the changing moment and shear envelopes. From a thermal point of view, analyzing these shaped slabs becomes a challenge to which heat transfer theory on extended surfaces offers models for a wide range of simplified geometries but falls short when studying more intricate geometries and boundary conditions. In response, this work proposes using conjugate heat transfer (CHT) simulations, a numerical method that allows studying any desired geometry through the discretized modeling of the solid and fluid domains.

These simulations aim to characterize the heat transfer process within and in the interfaces of the shaped cooling ceiling, to then translate these results into a whole-building simulation platform (section 3.3.). The CHT simulation settings follow the guidelines from previous work by Menchaca-Brandan [23], which have been applied and validated by author's prior work on the dynamic thermal performance of shaped thermal mass elements [3]. Air is modeled through the Boussinesq approximation, using the thermo-physical properties in Table 1. The RNG k-ε turbulence model, which describes turbulence using two

transport equations [46], is selected given its suitability and robustness for indoor airflow simulations with strong buoyancy flows [24]. Appendix B includes further details on the validation process based on experimental data from Olson et al. [41] and Blay et al. [42] for natural and mixed convection scenarios, respectively.

As shown in Fig. 5, the simulation domain consists of a 1.5-m cut of a 5-m-deep, 2.5-m-high apartment room, with only one façade exposed to the exterior air temperature (no solar radiation is considered at this point of the analysis but is included in 4.3). These dimensions provide a reasonable compromise between simulation time and flexibility for modifying, if necessary, the façade's boundary conditions and geometry. The floor and rear walls were modeled with adiabatic boundary conditions, as they are assumed to be sufficiently insulated and in contact with other apartments under similar room temperatures. The two remaining side surfaces are symmetry planes, which are equivalent to a zero-shear stress boundary throughout which there is no radiative nor convective heat flux.

The thermo-physical properties of the main bodies included in the CHT simulations are the following:

While the proposed CHT simulations account for the complex heat transfer interactions between the concrete slab and the surrounding air and surfaces, they do not include detailed modeling of the water pipes. As shown in Figs. 5 and 7, the plane within which the serpentine pipe is embedded is modeled as a uniformly cooled surface, permitting a coarser mesh for an already computationally expensive simulation. This cooling plane is, in essence, equal to the conductive layer with averaged temperature described in the general resistance method included in DS/EN ISO 111855–2 [25]. The standard serves as a starting point for the equivalence method described in the following section, which focuses on the thermal resistances between the mentioned cooling plane and the room's air and surfaces. It is assumed that the pipe's diameter and spacing are adequately dimensioned according to the application requirements described in section B.2. Of the standard.

3.3. Simulating shaped cooling ceilings in a BEM platform

In order to characterize the benefits that thermally activated shaped concrete slabs offer, it is important to model the annual energy use of a building with such a system compared to a baseline. An effective method for this is BEM, which typically does not natively support modeling complex geometries. This section describes the method utilized to translate the complex 3-D solid-fluid interactions captured by the CHT simulations into the 1-D heat transfer framework commonly used in BEM environments.

EnergyPlus (EP) is the default BEM environment used in this work. More specifically, the *Low Temperature Radiant System Model* offers the possibility of modeling water circuits as heat sources/sinks embedded in any surface inside the space of study. An equivalence model is proposed in which the behavior from the shaped concrete slabs matches a simplified 1-D concrete slab that can be then introduced into EP. As illustrated in Fig. 6, this equivalence is imposed for each of the three

Table 1
Thermo-physical properties of air, concrete and insulation as input in simulations [47]. NOTE: Boussinesq approximation treats density as a constant value except for the buoyancy term in the momentum equation.

	Density (kg/m³)	Specific heat (J/kg°C)	Thermal conductivity (W/m °C)	Emissivity	Coefficient of thermal expansion (1/C)	Dynamic viscosity (kg/m s)
Air	1.2 (boussinesq)	1007	0.025	–	0.0033	1.8×10^{-5}
Concrete (ceiling)	2400	900	1.2	0.9	–	–
Insulation (walls)	20	800	0.03	0.9	–	–
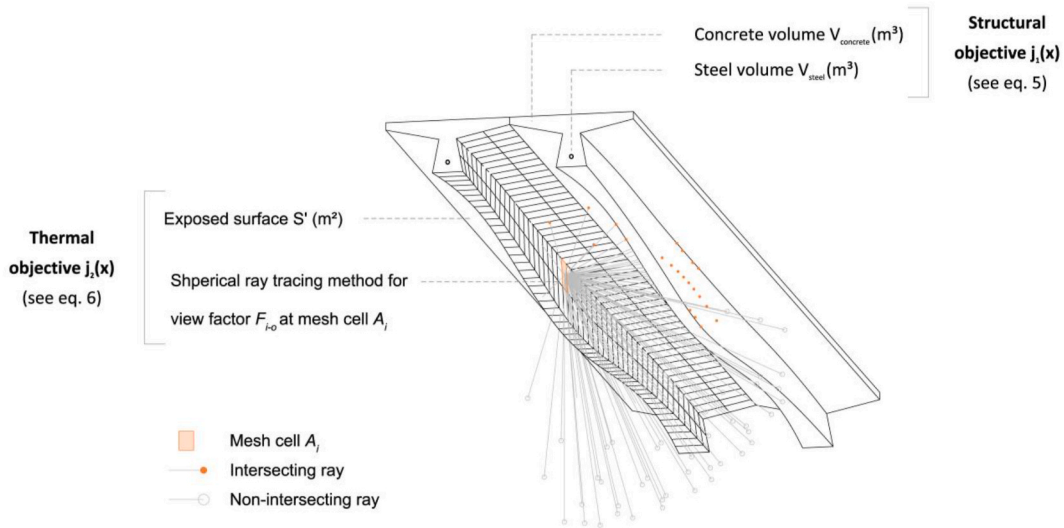
Fig. 4. Geometrical definitions input into the structural and thermal objectives defined in eqs. (5) and (6) respectively.
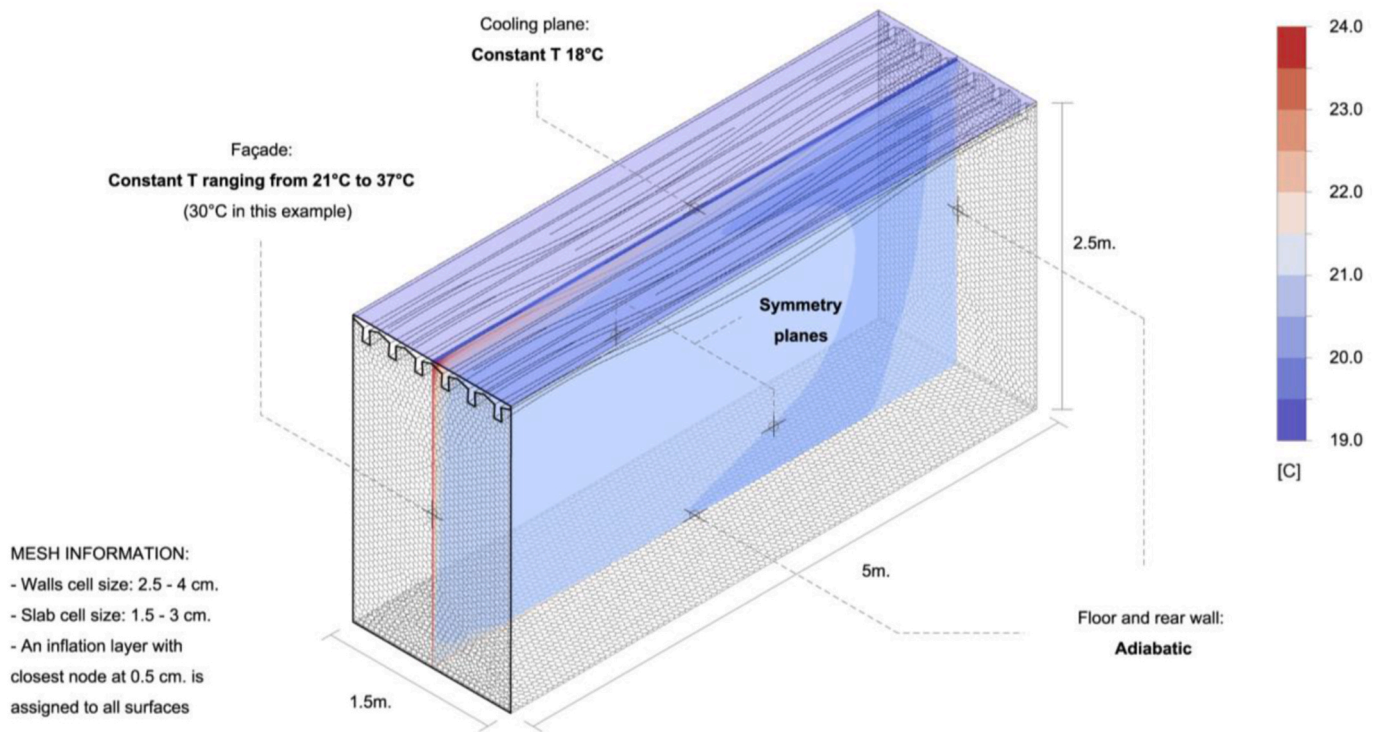
Fig. 5. Boundary conditions and basic mesh properties applied in the CHT simulations. For each façade temperature considered, simulations are run in transient mode until a steady-state is reached.

heat transfer processes in action: conduction (from the ceiling surface to the water pipes), convection (from the surrounding air to the ceiling surface), and radiation (between room surfaces).

3.3.1. Conduction

The embedded pipe depth L_1, measured from the slabs' surface, is a determining factor when sizing the cooling capacity of a conventional flat slab. For a given inlet water temperature $T_{w,i}$, the cooling capacity increases for smaller L_1 [26]. EnergyPlus captures this process by calculating the conduction resistance of the innermost concrete layer R_1. Similarly, an equivalent resistance R'_1 can be obtained from the CHT model by computing the temperature difference between the averaged

surface temperature $\overline{T}_s$ and water source T_w over the total conductive heat transfer rate:

$$R_1 = \frac{L_1}{k_1\,A} \tag{10}$$

$$R'_1 = \frac{\Delta T}{Q_{cond}} = \frac{(\overline{T}_s - T_w)}{Q_{conv} + Q_{rad}} \tag{11}$$

The goal then becomes to find the equivalent L'_1 so that the steady-state resistance used in the whole building model is equal to the one obtained from the CHT calculation. This method naturally involves simplifying the actual 3D behavior of the slab, as averaging the surface
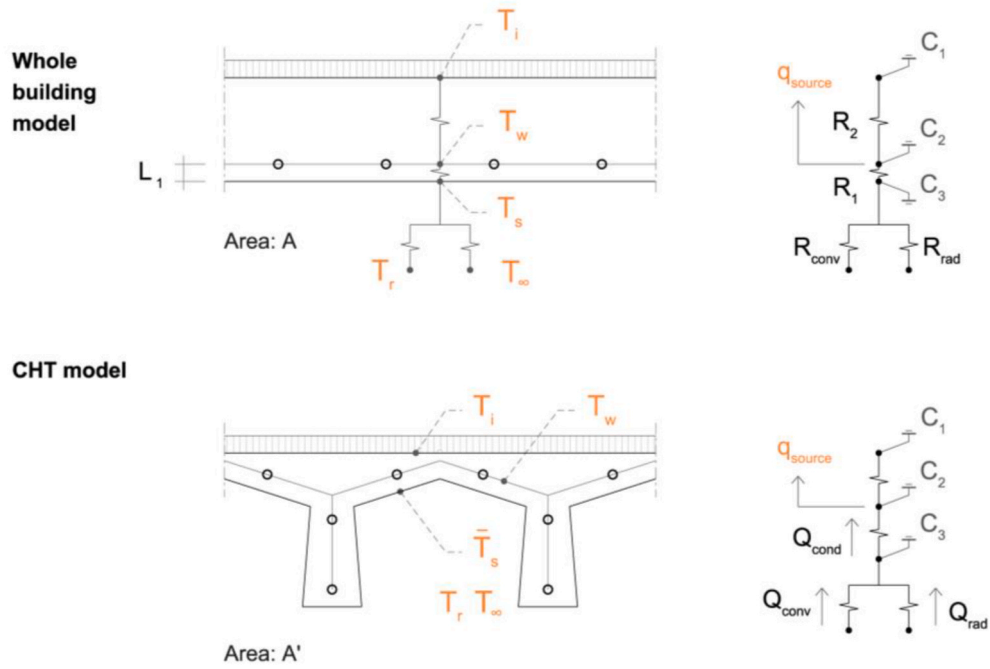
Fig. 6. Thermal circuit equivalence established between the whole building and CHT models. The values for R_1, R_{conv} and, R_{rad} are matched with the resistances obtained from Q_{cond}, Q_{conv}, and Q_{rad}.
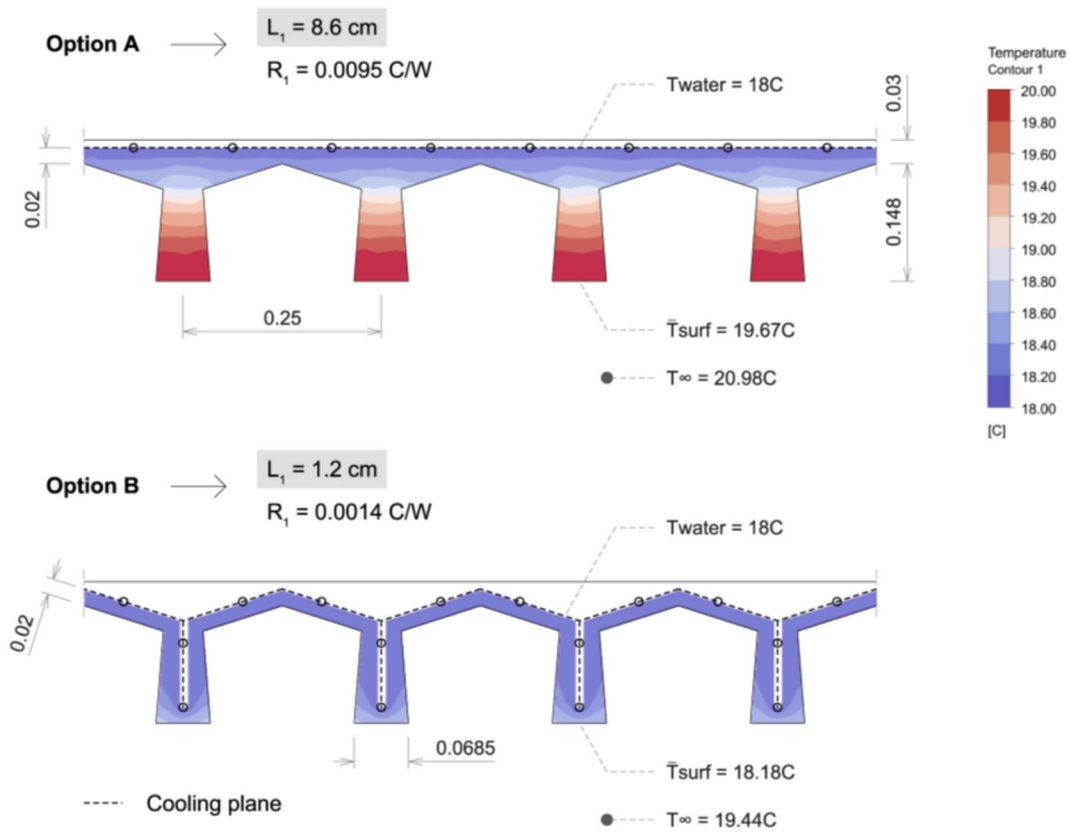
Fig. 7. Equivalent thickness L'_1 and temperature distribution at steady state computed for a horizontal cooling plane (option A) and a shaped, parallel to the celing, cooling plane (option B).

temperature prevents accounting for local phenomena. However, the importance of such temperature variations will vary across water pipe layouts, as shown in Fig. 7.

$$L_1' = \frac{k_1 A \left(\overline{T}_s - T_w\right)}{Q_{conv} + Q_{rad}} \tag{12}$$

Fig. 7 shows two possible configurations for the same shaped geometry: option A presents a horizontal layout across the slab's top flange, while option B has a shaped pipe distribution parallel to the ceiling. The same room size and boundary conditions are applied for both cases. As expected, option B results in a much thinner equivalent thickness L_1, as well as a more homogenously distributed temperature surface. Option A instead translates into a thicker 8.6 cm equivalent slab due to the conduction resistance added by the concrete ribs. In this case, the temperature distribution resembles a rectangular fin with a 1-D temperature gradient from the flange's base down to the rib's tip. Given the reduced thermal resistance and consequent faster activation time, option B will be the water pipe layout used in this work moving forward. Finally, the dynamic thermal performance of the shaped slab is modeled by matching the total heat capacity of each concrete slab. This process has proved satisfactory for the single-material floor systems studied in this research, as shown in the validation data included in Appendix A. More complex multi-material structures, such as a beam and block slab system, could be analyzed through, for example, the structure factor method [27].

3.3.2. Convection

The slab's geometry strongly determines the convective heat exchange between the ceiling surface and surrounding air through changes in the exposed surface area and orientation. This air film resistance is modeled in EnergyPlus as:

$$R_{conv} = \frac{1}{h \, A} \tag{13}$$

Once again, it is possible to find an equivalent resistance R'_{conv} from the steady-state CHT simulations by extracting the convective heat transfer rate and temperature difference of interest. The air temperature T_∞ is computed as the room's volume-average temperature, in accordance with the perfectly mixed air assumption used in the whole building energy model.

$$R_{conv}' = \frac{\Delta T}{Q_{conv}} = \frac{(T_\infty - \overline{T}_s)}{Q_{conv}} \tag{14}$$

In this case, the objective is to find an equivalent heat transfer coefficient (HTC) h'_c for the convective resistance modeled in EnergyPlus that matches the one from the numerical simulation. Although not common in heat transfer references, the calculation of h'_c is normalized by floor area so that the performance of each ceiling geometry is effectively transferred into the whole-building simulation platform. This process is repeated for multiple ΔT, resulting in two temperature-dependent heat transfer coefficient functions (heating and cooling) for each geometry (Fig. 8). Liu et al. [28] follow a similar strategy for quantifying the impact of the exterior convective HTC on building energy consumption.

$$h_c' = \frac{Q_{conv}}{A_{floor} \left(T_\infty - \overline{T}_s\right)} \tag{15}$$

These new equations are introduced manually in EnergyPlus using the Adaptive Convection Algorithm, a mechanism included in the BEM tool to dynamically select the relevant HTC function based on the surface type and flow regime. This method, initially developed by Beausoleil-Morrison [29], presents a series of default convective heat transfer equations identified from the literature while also allowing users to input new correlations. In the case of actively cooled ceilings, the adaptive algorithm uses numerical results obtained by Karadag [30] for multiple room configurations. Similarly, Alamdari and Hammond [31] developed correlations based on experimental data for horizontal surfaces under buoyancy-driven convection. In both cases, the h equations are defined by an exponential function of the following shape:

$$h = C_1 \, \Delta T^{C_2} \tag{16}$$

The sparse data outputted by the CHT simulations is fitted using a
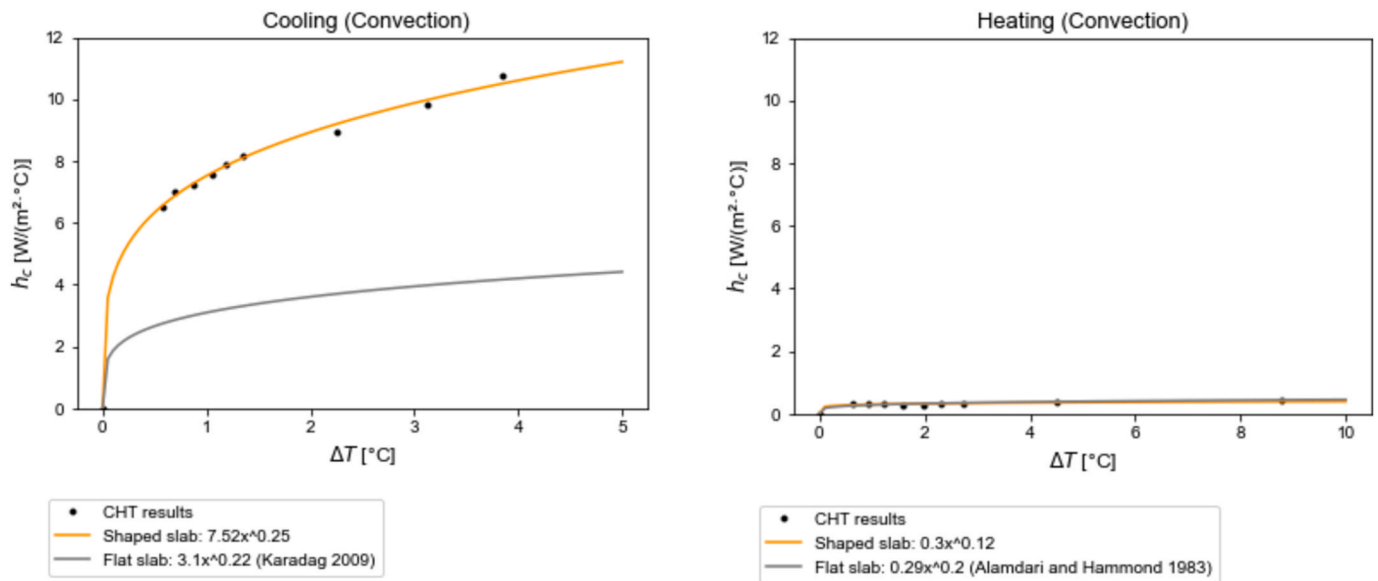
Fig. 8. Convective heat transfer coefficient curves for the flat and shaped slabs of study. The air stratification and dynamics of the buoyancy forces lead to an asymmetric performance in which the shaped slab only improves its convective performance in cooling mode.

power function with the corresponding values for C_1 and C_2. Fig. 8 shows the correlations found for the example geometry in both cooling and heating scenarios. As observed, the shaped slab provides significantly higher cooling heat transfer coefficient values h'_c compared to the literature values for flat ceilings. This behavior mainly results from the increase in exposed ceiling surface per square meter of projected floor area, which in this case increases from 1 m^2/m^2 to 2.34 m^2/m^2. Conversely, the performance of both solutions is identical in a heating setting. As shown in previous studies on the thermal mass performance of shaped slabs [3], the accumulation of hot stratified air in between the concrete ribs prevents the shaped ceiling from taking advantage of its extended surface when warmer than the surrounding air. These new HTC values are defined as a function of ΔT and are therefore only valid for buoyancy ventilation cases. The inclusion of forced ventilation would require the definition of a new set of equations that have not been included in this work.

3.3.3. Radiation

Radiative heat transfer plays a key role in the radiant ceiling's performance, accounting in most cases for more than 50% of the total cooling capacity [32]. As identified by literature reviews on surface heat transfer coefficients, a constant heat transfer coefficient h_r of 5.5 $W/m^2°C$ is a safe assumption for flat radiant ceilings in common room configurations with high emissivity surfaces [33]. In the context of this work, h'_r is obtained by dividing the radiative heat transfer rate Q_{rad} over the temperature difference and is, once again, normalized by the room's floor area.

$$h'_r = \frac{Q_{rad}}{A_{floor}\,(T_{AUST} - \overline{T}_s)} \tag{17}$$

The average unheated surface temperature (T_{AUST}) is calculated for a reference horizontal plane using the following definition. View factors from the ceiling of interest to the surrounding surfaces j are extracted from the numerical models:

$$T_{AUST} = \sqrt[4]{\sum_{j=1}^{n}\left(F_{s-j}T_j^4\right)} \tag{18}$$

The CHT results reveal that the radiative heat transfer coefficient has almost no variation between flat and shaped geometries. Fig. 9 shows how the fitted data is strongly aligned with the mentioned 5.5 $W/m^2°C$ for horizontal ceilings. These results agree with the conclusions obtained by Grinham et al. [12]: as the exposed surface increases, the ceiling's view factor to the surrounding surfaces diminishes because of the rib's self-shadowing, creating a counteracting effect between both phenomena. The high emissivity associated to the concrete surfaces (0.9) also contributes to this similarity across results.

Very similar values are obtained for all the other geometries modeled in this study. Given that the variations observed are in the order of 3–4% relative to the reference flat ceiling (and always in the conservative side, i.e., with slightly higher heat exchange for geometries with higher TF), all shaped slabs are modeled in EnergyPlus using the default radiation analysis configuration. This similarity in the radiative performance between shaped and flat slabs should be validated for any other generated geometry, paying particular attention to those with lower emissivity values.

4. Results

The following lines show the process to identify and analyze five designs for optimal structural-thermal concrete slabs, using the methods described in the previous section.

4.1. Geometry selection

Fig. 10 shows all the designs from the last generation explored by the NSGA-II algorithm, coloring those belonging to the Pareto front. The graph also highlights the geometries that are selected for the CHT analysis, two of which (v1 and v5) are the single-objective optimal designs for $J_1(x)$ and $J_2(x)$ respectively.

To obtained these results, the genetic algorithm was set up using the
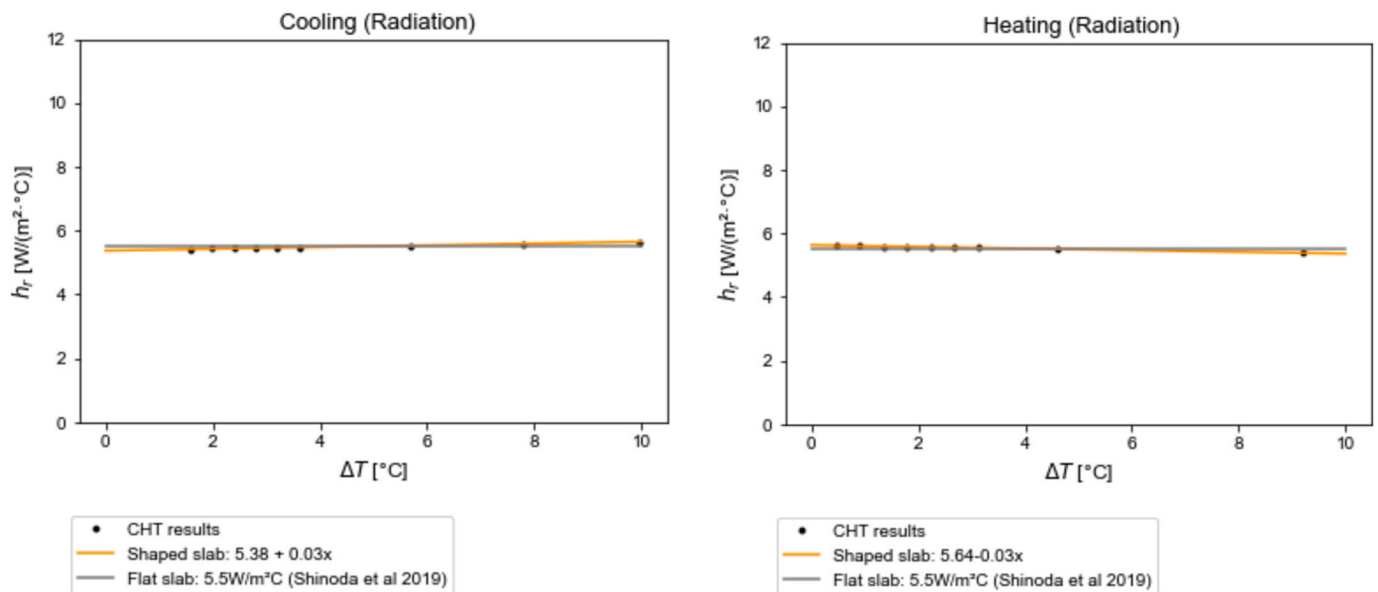
Fig. 9. Radiative heat transfer coefficient curves for the flat and shaped slabs of study. The surface increment in the shaped slab is balanced by its self-shadowing, leading to an almost identical radiation h.t.c. curve relative to the 5.5W/m ^{2}C literature value for flat geometries.
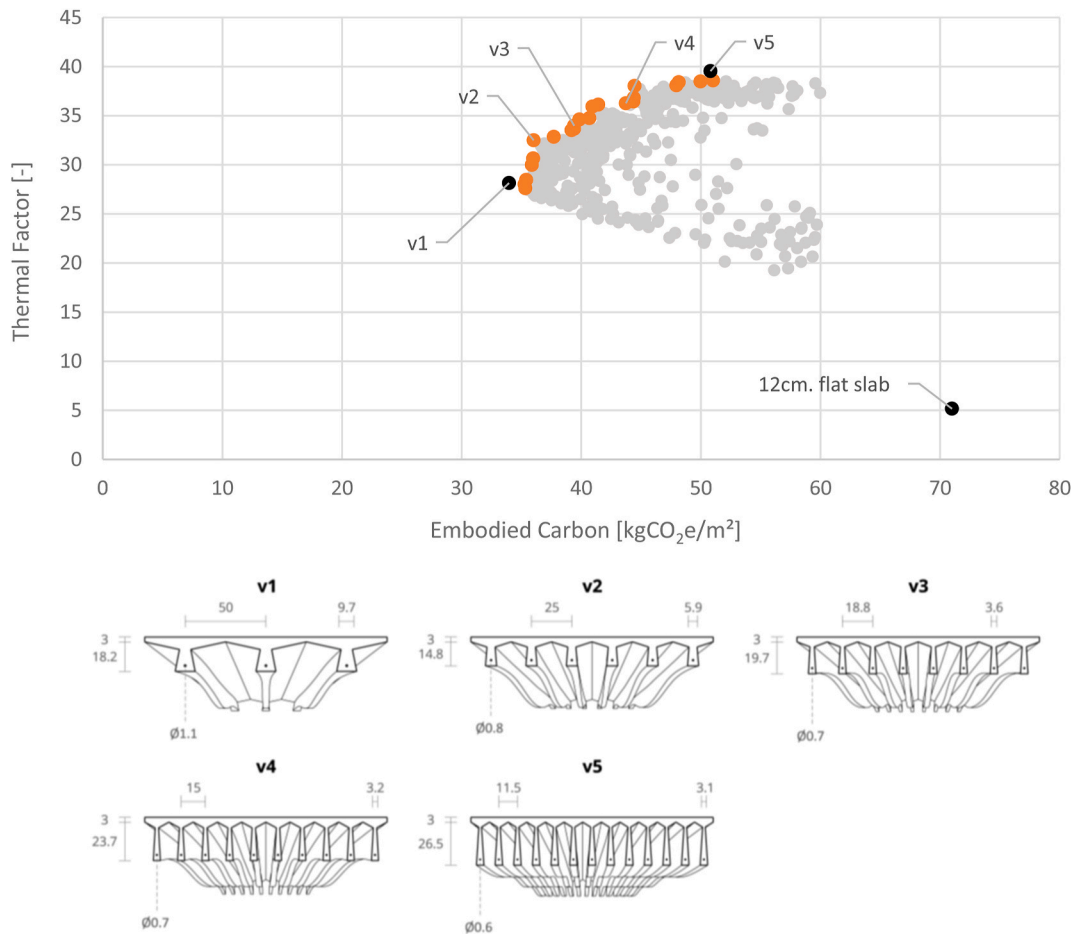
Fig. 10. Pareto front for thermal factor and embodied carbon (top) and selected geometries for CHT analysis (bottom). Concrete slabs and steel reinforcement dimensions are in cm.

Table 2

Genetic algorithm parameters, as defined in the Design Space Exploration toolbox [20]. w1 and w2 refer to the thermal factor definition defined in equation (6).

	Population size	Generations	Random seed	w1	w2
NSGA-II parameters	800	60	1.15	0.5	1.0

parameters shown in Table 2.

The shape of the obtained Pareto front reveals a clear tradeoff between the thermal and structural performances, with embodied emissions ranging from 33.9 to 50.8 kgCO$_2$e/m^2 and the thermal factor from 28.1 to 39.5. A first glance into the selected geometries shows how *x1*, the distance between ribs, is one of the most influential variables when moving along the Pareto curve. Indeed, by bringing the ribs together, the exposed surface and TF increase to the detriment of the structural mass, which unavoidably augments. It is also interesting to observe how the design of slabs with larger ribs spacing is moment-dominated (v1 and v2), whereas shear stresses have a larger impact on the geometry of slabs with closer ribs (v4 and v5). The bi-objective plot also helps identify that all Pareto designs surpass the 12 cm optimal flat slab in both objectives, presenting promising structural-thermal advantages. All the designs satisfy the described structural constraints under a live load of 200 kg/

m^2 (2 kN/m^2), a common value for residential buildings. The embodied carbon calculation was performed using baseline values defined by the Carbon Leadership Forum for both stainless steel (3 kgCO$_2$e/kg) and concrete (0.15 kgCO$_2$e/kg) [34]. This serves as a first approximation to the context-specific analysis conducted in Section 4.3.

4.2. Heat transfer performance characterization

This section summarizes the heat transfer performance computed for each of the five geometries selected from the Pareto front. All cases are modeled assuming a water circuit uniformly distributed along the ceiling surface. Table 3 summarizes all the values for the constants C_1 and C_2. In alignment with the results from Section 3.3. the convective heat exchange increases thanks to the progressive increment in ceiling area from slabs v1 to v5.

Table 3

Constants C_1 and C_2 for each geometry's cooling htc exponential curve, as defined in equation (15).

	Flat	v1	v2	v3	v4	v5
Constant C_1	3.11	4.05	7.52	11.77	16.1	28.89
Constant C_2	0.22	0.28	0.25	0.28	0.3	0.33
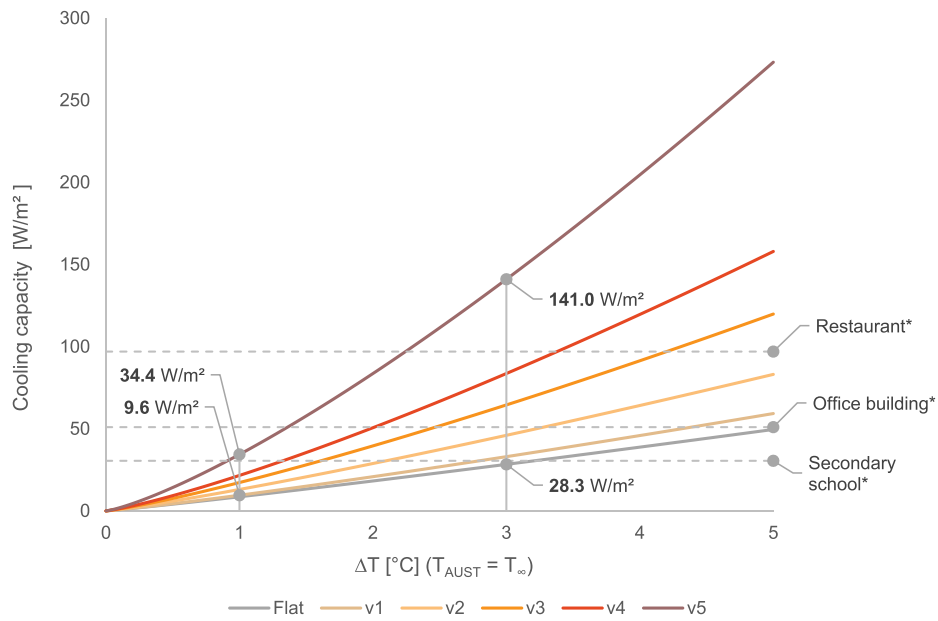
Fig. 11. Ceiling cooling capacity as a function of ΔT for all five geometries of study. The horizontal lines correspond to reference peak cooling demands obtained from ASHRAE 90.1 EnergyPlus templates.
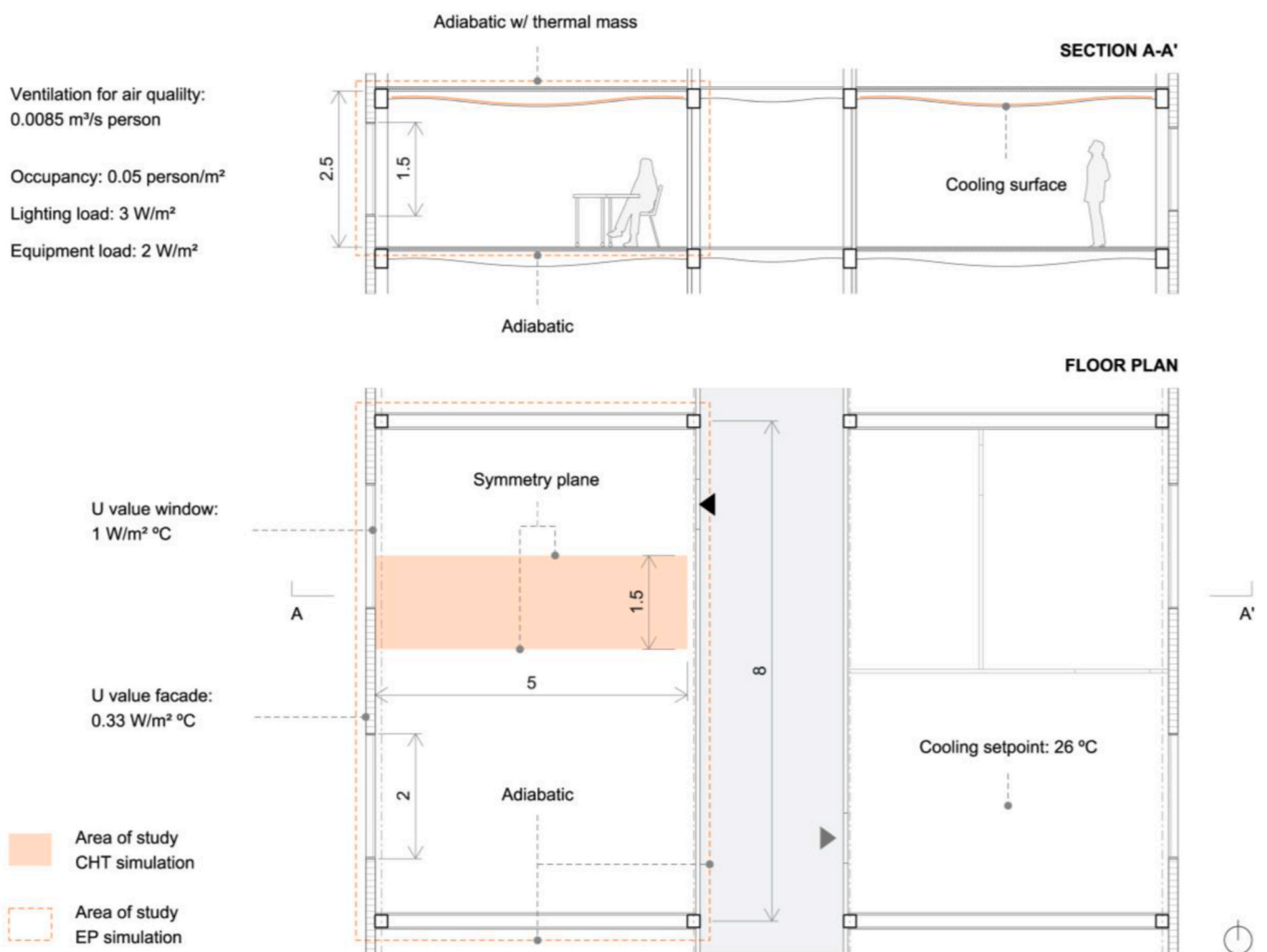
Fig. 12. Case study of a prototype 8 × 5m west-facing apartment with highlighted boundary conditions for CHT and EP simulations. All dimensions are in m.

The total cooling capacity can be then calculated with the following expression for conditions in which T_{AUST} and T_∞ are the same:

$$q = \left(h_c' + h_r'\right)\Delta T \tag{19}$$

Fig. 11 shows how the thermal factor (TF) metric has successfully predicted the best performing geometries. As ΔT and TF increase, the cooling capacity of the radiant ceiling also increases. Two clear advantages are evident from these results. First, slabs with higher TF can reach any cooling capacity value with warmer water temperatures. This effect could lead to higher chiller efficiencies and reduced condensation risks (see Section 4.3). Second, the improved performances allow for expanding the use of these systems in building typologies that traditionally have higher peak cooling demands. Fig. 11 includes multiple reference peak values extracted from ASHRAE 90.1 EnergyPlus templates. As observed, the demands that correspond to more intensive uses (restaurant, offices) can only be met by slabs with high TF.

Finally, the dynamic thermal performance of the selected designs was also assessed with the objective of analyzing their passive behavior when not thermally activated. This study follows the methods proposed by the authors in previous work [3], consisting of transient CHT simulations in which the damping coefficient (difference between peak outdoor and indoor temperatures) is measured after a 24-h cycle. The damping coefficient was slightly increased, between 6 and 9%, for all five geometries, as shown in the temperature plot in Figure A2 (Appendix A). These results confirm the initial conclusions: it is possible to remove structural mass (up to 55% in this case) from concrete floor
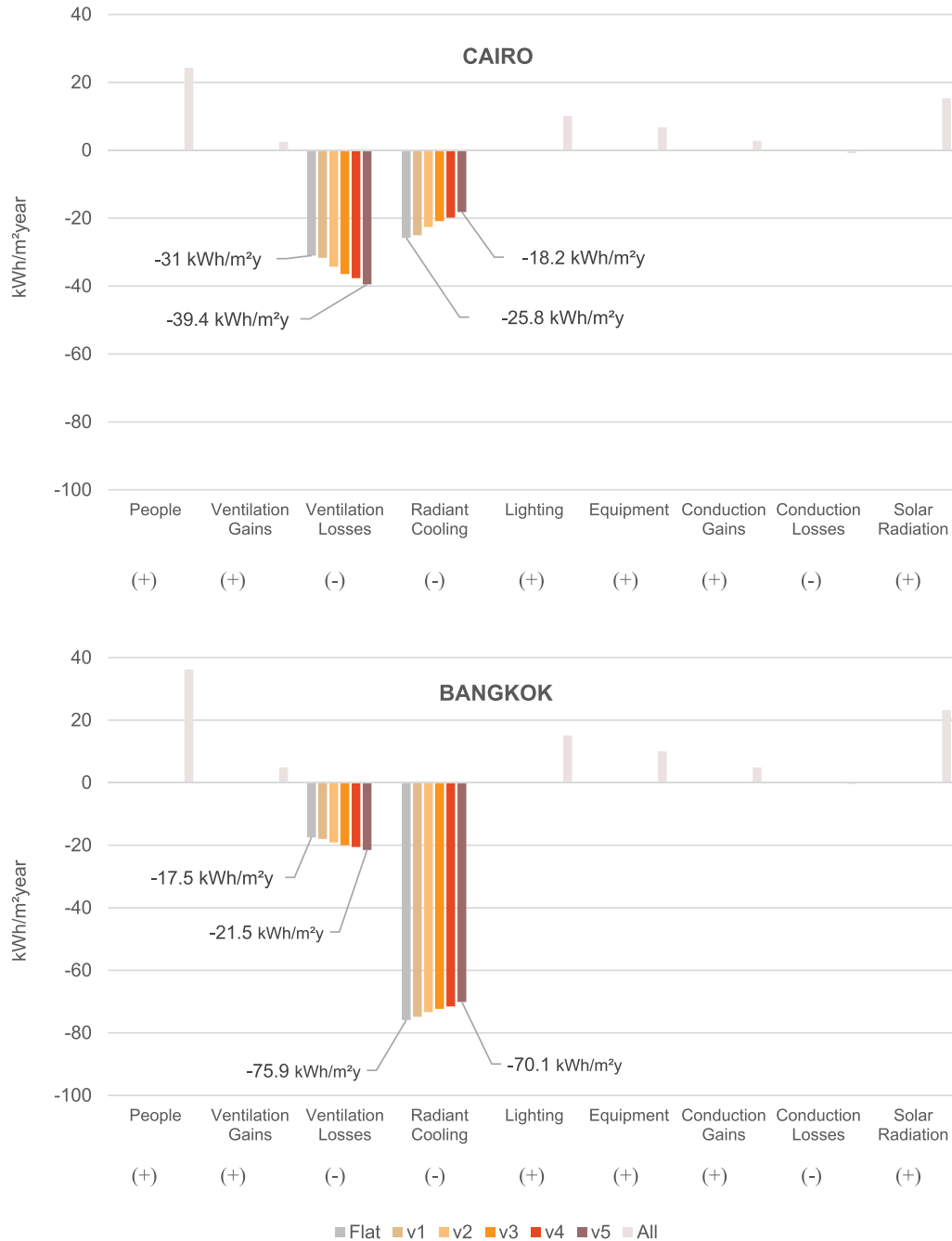
Fig. 13. Energy balance for both climates of study. Bars with (+) correspond to energy incoming into the system and those with (−) indicate energy extracted out of it.

systems without affecting their dynamic thermal mass performance.

4.3. Case study: concrete floor systems in low-carbon apartments

This final study aims to evaluate the environmental performance of the five selected concrete geometries on a prototypical apartment unit across two representative climates. Cairo is chosen as the hot desert climate, with 900 annual cooling degree days (CDD) and mean daily temperature fluctuations of 11.5 °C, and Bangkok as tropical wet, with 2042 CDD and daily fluctuations of 9.2 °C. The proposed case study consists of a west-facing 8 m × 5 m apartment unit accessed through a central access corridor, as illustrated in more detail in Fig. 12.

The main features of the whole-building simulations are the following:

- An active cooling system with a constant-flow radiant ceiling is embedded in the concrete structure. Water is supplied at temperatures ranging from 16 °C to 21 °C.
- Simple fan-driven ventilation controls the air exchanges for air quality, with no pre-conditioning or heat recovery processes. Natural ventilation is enhanced whenever outdoor conditions are within comfort ranges, fostering night-flush ventilation in climates with large diurnal temperature fluctuations.
- Thermal comfort is characterized in all simulations using the PMV method, considering a metabolic rate of 1 met and a clothing level of 0.5 clo. The addition of a ceiling fan provides a constant indoor air speed of 0.4 m/s when necessary.
- Dehumidification is considered only for condensation-prevention purposes but not for comfort, as this is achieved exclusively through the cooling ceiling and fans.
- The same envelope configuration, occupancy schedule, and internal loads are used for both climates studied. While these values may vary across locations, assuming a default configuration is considered sufficient for the early-stage scope of this study.

As observed in Fig. 13, geometries with higher thermal factors decrease their annual cooling demand while providing comfort in all cases thanks to the higher convective heat transfer coefficient h'_c. This faster thermal response means the embedded radiant system "invests" less energy in pre-cooling the floor's mass, increasing slab temperatures as the thermal factor increases. As a result, night-flush ventilation becomes essential to passively remove this extra energy that the radiant system has not extracted. Fig. 13 shows how the heat dissipated through ventilation increases as the cooling demand decreases, balancing the annual energy loads. Climates that are more suited for a passive thermal mass strategy (i.e., high diurnal fluctuations with mean temperatures close to comfort ranges) will benefit more from this strategy, as the possibilities of night-flushing will be higher. For this reason, the apartment in Cairo presents higher reductions in cooling demand (29.5%) compared to the one in Bangkok (7.5%).

Additionally, ceiling geometries with higher thermal factors have lower condensation risk as they achieve thermal comfort through warmer surface temperatures. While this is not relevant for Cairo's dry climate, where no condensation occurs, it is for Bangkok's: the total degree-hours during which the ceiling's temperature is below the 1 °C

offset dew point is reduced from 6302 for the flat slab to 2656 for geometry v5. This results in an equivalent decrease in the latent load Q_{lat}, which is computed post-simulation using the following expression:

$$Q_{lat} = \rho_{air} \, L_{we} \, \dot{V} \Delta w_{kg} \tag{20}$$

The total electricity consumption expressed in Table 4 is obtained by dividing the removed latent heat by the system's coefficient of performance COP_{lat}. For this analysis, an isothermal membrane-based air dehumidification (IMAD) system is chosen, assuming a COP_{lat} of 2 (a reasonable value according to the available literature, with COP_{lat} ranging between 0.75 and 3 [35]). This solution presents promising low energy performances thanks to having no need of overcooling air for condensation.

Finally, the required pumping power was approximated using the mass flow rates obtained from the whole-building simulations and the Hagen-Poiseuille expression for the pressure drop. Slabs with larger ceiling areas present, as expected, higher losses given their added piping length per m^2 of floor area. However, they also provide comfort with slightly lower flow velocities thanks to the enhanced thermal performance, counteracting to some extent the first effect. The pump's energy consumption increases from 0.05 (flat) to 0.08 kWh/m^2year (shaped v5) which, in absolute terms, is considered negligible compared to the final energy consumption required by the chiller (70.1 kWh/m^2year).

4.4. Carbon assessment

Once the operational energy consumption and material volumes have been computed, a 50-year lifespan carbon assessment is developed for each concrete floor design. The carbon intensity of electricity (kg CO_2e/kWh) results from combining available data on the electricity mix of the countries considered [36] with reference values of the carbon intensity for each energy source [37]. The embodied carbon coefficients (kg CO_2e/kg) for concrete and stainless steel are selected from the EC3 database, an open-access tool based on third-party verified Environmental Product Declarations [38].

Fig. 14 reveals multiple trends:

- Embodied carbon plays a decisive role in climates with moderate cooling demands like Cairo's. This makes geometries with higher structural performance, such as v1 and v2, suitable options when considering short and mid lifespans.
- Conversely, operational carbon dominates in climates where the cooling demand is higher. For example, in Bangkok, the best thermally performing design (slab v5) becomes the least carbon-intensive option after only 8 years.
- Shaping radiant cooling ceilings is a carbon-efficient strategy from the day of construction due to the initial embodied carbon reduction. The cumulative savings increase to 31.5% and 22.3% for Cairo and Bangkok respectively, compared to flat solutions.
- These savings increase further when put alongside more conventional cooling options, such as window AC units. After 50 years, slab v5 achieves a reduction in the total carbon emissions of 68.5% for Cairo and 40% for Bangkok.

The results plotted in Fig. 14 are also sensitive to other variables independent of the slab's geometry, such as the chillers and membrane COP or the electricity carbon intensity. These parameters could vary across projects and consequently alter the slope of the emission lines. It is then important to note that the conclusions obtained here are only valid for these specific analyzed cases, requiring new simulations every time. Along similar lines, these calculations could be fine-tuned in future work by accounting for the morphing of the climate and the future decarbonization of the electricity grid.

Moreover, the distribution of embodied and operational emissions across geometries is consistent with the performance tradeoffs found in

Table 4
Estimation of the electricity consumed by the Isothermal Membrane-based Air Dehumidification (IMAD) system. As the thermal factor increases, the condensation risk (and corresponding latent demand) diminishes.

	Flat	v1	v2	v3	v4	v5
Degree-hours Tsurface < Tdew+1	6302	5540	4190	3526	3177	2656
Latent heat removed (kWh/year)	642.5	568.1	434.7	368.2	332.9	279.9
Electricity consumption (kWh/m^2year)	8.03	7.1	5.43	4.6	4.16	3.5
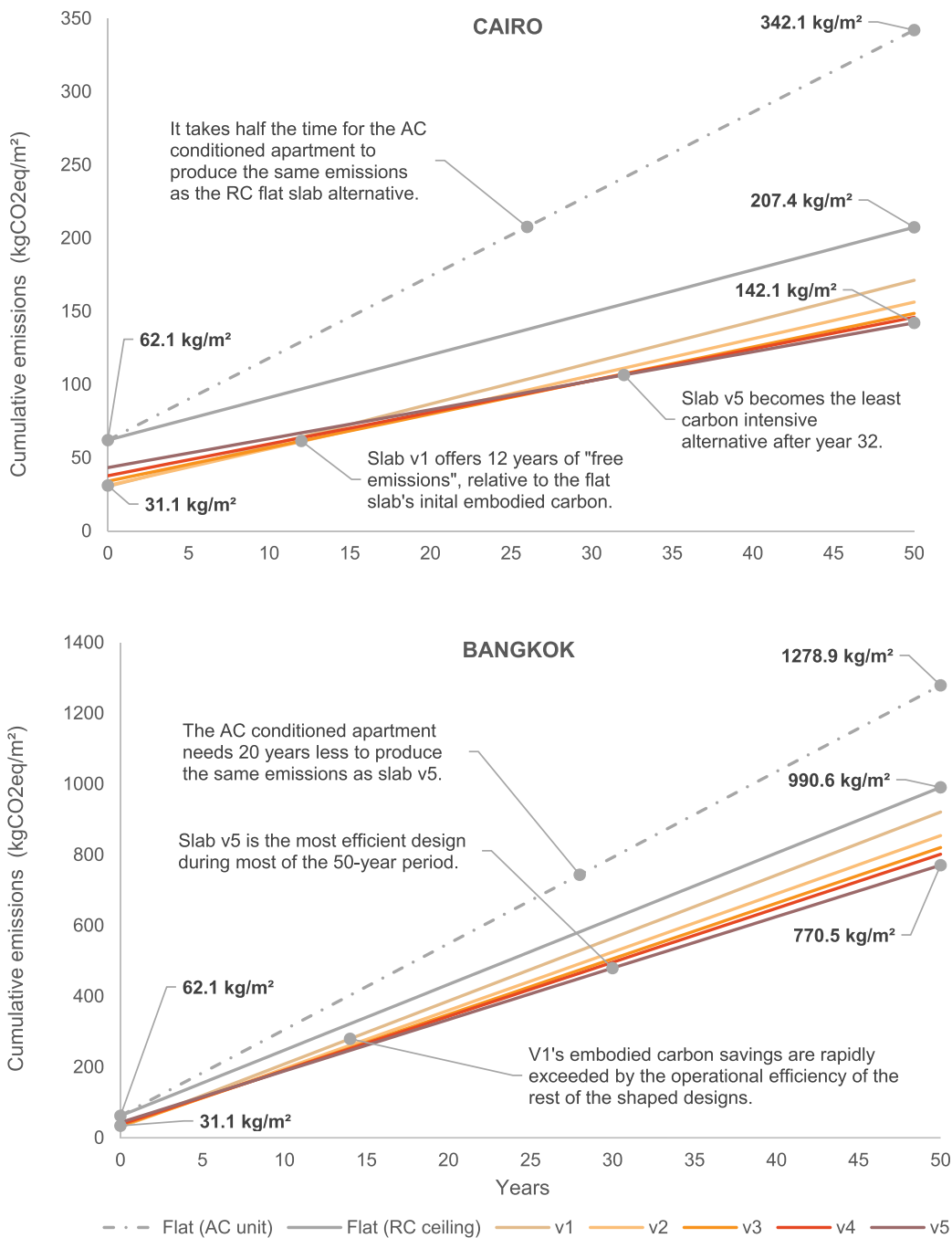
Fig. 14. 50-year lifespan carbon assessment. Slabs with lower embodied emissions are more suitable for Cairo (v1,v2), whereas, in Bangkok, those with improved thermal performance (v4,v5) are preferable. Note: RC refers to Radiant Cooling, and AC to Air-Conditioning.

the initial Pareto front, reinforcing the potential of MOO methods as an early-stage design tool. Fig. 15 reveals how, as the embodied footprint of the concrete slabs decreases, their operational impact increases for all years and climates considered. It is also interesting to observe how the Pareto fronts progressively widen over time as the impact of the operational carbon increases relative to the embodied footprint.

5. Conclusions

Recent research on structural optimization offers innovative shape optimization methods for the design of lightweight concrete structures that achieve outstanding material savings. At the same time, radiant cooling ceilings are emerging as a strong alternative to conventional

space conditioning systems thanks to their user-centric approach to thermal comfort. This research lies in the intersection of both worlds, proposing new methods to design and evaluate shaped floor elements that optimally perform as both load-carrying structures and thermally activated surfaces.

5.1. Summary of contributions

The multi-objective optimization techniques presented in this work allowed finding floor geometries that outperform conventional flat slabs structurally and thermally. For instance, shaped slab v2 significantly reduces its embodied carbon by 50% while achieving annual operational savings of 14% (Cairo) and 12% (Bangkok) relative to prismatic floors.
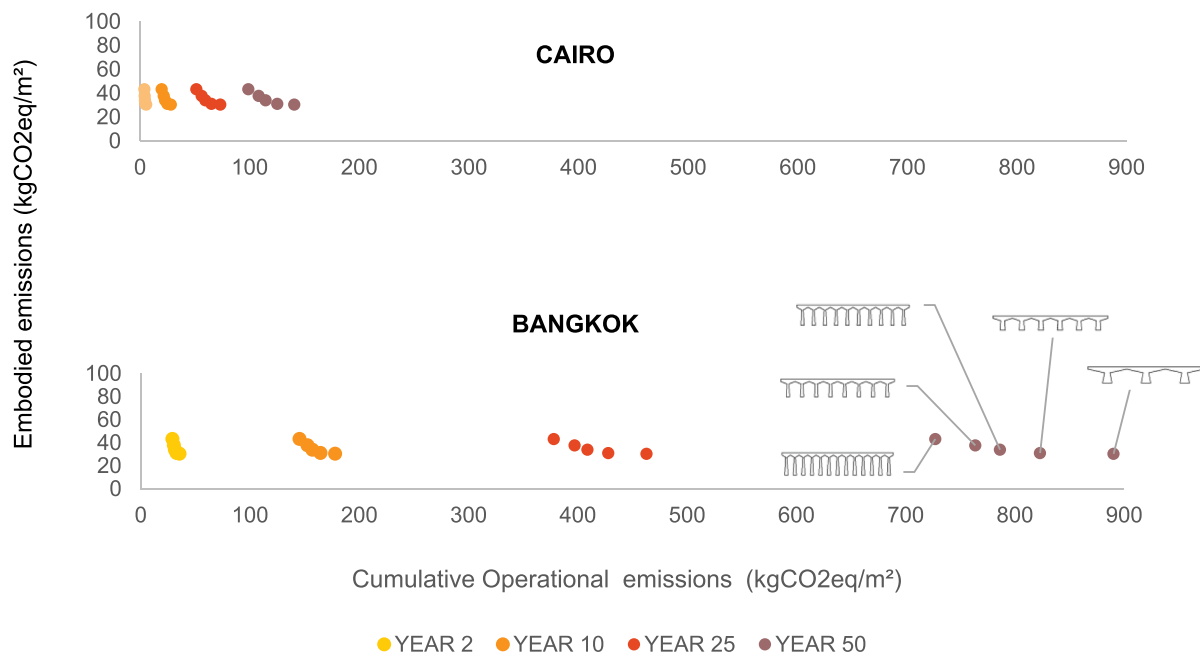
Fig. 15. Updated Pareto front by plotting cumulative operational and embodied emissions. The embodied-operational tradeoff remains throughout the building's lifespan, increasing the relative impact of the operational emissions throughout time.

On the other end of the obtained Pareto front, v5 reaches higher operational reductions of 32% (Cairo) and 22% (Bangkok) at the expense of lowering the embodied savings to 30%. These results highlight the validity of the new thermal factor metric in computational design frameworks as an analytical way of characterizing the thermal performance of the rigorously shaped radiant surfaces.

This research also offers new preliminary results related to the energy-efficiency advantages of shaped concrete TABS. Ceilings with higher thermal factors improve their cooling capacity thanks to the increased convective heat transfer h'_c, overcoming a recurrent sizing limitation in conventional flat systems. Results show performance enhancements of up to 34.4W/m^2 when $\Delta T = 1\ ^\circ C$ and 141 W/m^2 when $\Delta T = 3\ ^\circ C$, values within the ranges identified in the literature review [11–13]. Further, the increased convective heat transfer translates into energy savings on an annual basis. This is particularly true for climates in which night-flush ventilation can be used effectively, reaching a reduction of up to 29.5% for Cairo's cooling demand. Finally, the risk of condensation also diminishes for shaped cooling ceilings, given their ability to reach the same cooling capacity with warmer water temperatures. The energy consumed for dehumidification (approximated for a membrane system) was diminished by 56% for slab v5, relative to the flat ceiling. While recent developments in radiant technologies can reach higher cooling capacity values (through, for example, flat heat pipes [39]) or improved condensation control (through cover shields [40]), shaped concrete ceilings offers an integrated, easy-to-implement alternative with combined embodied and operational carbon savings.

From a methodological point of view, this paper presents a first approach to modeling shaped, thermally activated building elements in BEM platforms. Using the work from Strand and Baumgartner as a starting point [41], the introduction of an equivalent flat slab offers an easy-to-implement and flexible tool that allows computing the operational energy consumption of any desired geometry. This equivalence was validated by comparing CHT transient simulations with the result obtained from the whole-building simulation (see Appendix A).

5.2. Limitations and future work

The proposed work includes a series of simplifications that, in order to broaden its applicability, need to be approached in future work. First, the equivalent flat slab method currently only supports the modeling of high-emissivity surfaces and should be expanded to more reflective ceilings that might not present a constant h_r value. Similarly, the multi-objective optimization framework presented in this work could be further refined by including physical insights on heat transfer theory on finned surfaces (adding, for example, new constraints or fine-tuning the 'thermal factor' definition). This process would result in two combined advantages: first, potentially reducing the required computational time to find the Pareto fronts, and second and most importantly, providing analytical benchmark designs that could inform early-stage design processes. Other avenues to explore in future work include the consideration of temperature gradients across the ceiling surface for local discomfort calculations and the inclusion of forced ventilation scenarios.

5.3. Concluding remarks

The in-progress construction of a slab prototype will allow exploring construction methods that are as replicable and easy-to-implement as possible. Early tests are already revealing further opportunities for integration, such as the combined use of steel pipe as reinforcement and water tubing. Answering these and other implementation questions will be essential to achieve the scalability of these systems as a tool to mitigate climate change and provide effective adaptation solutions.

CRediT authorship contribution statement

Eduardo Gascón Alvarez: Writing – original draft, Visualization, Software, Methodology, Investigation, Data curation, Conceptualization. **Natasha L. Stamler:** Writing – review & editing, Software, Data curation, Conceptualization. **Caitlin T. Mueller:** Writing – review & editing, Supervision, Funding acquisition, Conceptualization. **Leslie K. Norford:** Writing – review & editing, Supervision, Funding acquisition, Conceptualization.

Declaration of competing interest

The authors declare that they have no known competing financial interests or personal relationships that could have appeared to influence the work reported in this paper.

Data availability

Data will be made available on request.

Nomenclature

A	Area of mesh cell, projected floor area (m^2)
ECC	Embodied Carbon Coefficient ($kgCO_{2eq}/kg$)
F	view factor
g	constraint function
h	heat transfer coefficient ($W/m^2\,°C$)
h'	equivalent heat transfer coefficient normalized by floor area ($W/m^2\,°C$)
J	objective function
k	thermal conductivity ($W/m\,°C$)
L_{we}	latent heat vaporization water (J/kg)
p	penalty function
q	cooling capacity, heat flux (W/m^2)
Q	eat transfer rate (W)
R	thermal resistance ($m^2\,°C/W$)
StV	surface to volume ration (m^2/m^3)
T	temperature (°C)
V	volume (m^3)
$\dot{V}$	air volume flow (kg/m^3)
w_{kg}	humidity ratio (kg water/kg dry air)
w	weight for thermal factor calculation
ρ	density (kg/m^3)

Subscripts

AUST	average unheated surface temperature
cond	conduction
conv	convection
floor	projected floor area
i	inlet, indoor or design *i*
lat	latent
rad	radiation
s	ceiling surface
o	outlet
w	water

Appendix A

Section 3.3 presents an equivalence method that allows transferring the complex thermal performance of shaped cooling ceilings into available BEM platforms such as EnergyPlus. This appendix includes the data collected to validate this method. A series of CHT and EnergyPlus simulations were performed under the exact same boundary conditions to compare the dynamic thermal response of the five geometries selected in Section 4.1. The input data introduced in both models is the following:

- Room dimensions: $5 \times 10 \times 2.5$ m. All surfaces are adiabatic, with the exception of one 2.5×10 m façade.
- Boundary conditions: a sinusoidal temperature curve is imposed in the façade's outer face, as a representation of a daily temperature fluctuation. Two "climates" are analyzed:
  o *C1: T(t) = 31.55[C] – 3.55[C]* sin *(2πt/86400[s])*
  o *C2: T(t) = 30.95[C] – 5.75[C]* sin *(2πt/86400[s])*
- No solar radiation or internal gains are considered.
- Material properties:
  o Concrete: 2400 kg/m^3, 1.2 W/m°C, 880 J/kg°C.
  o Insulation: 20 kg/m^3, 0.03 W/m°C, 800 J/kg°.C.
- All surfaces have a thermal emissivity of 0.9.
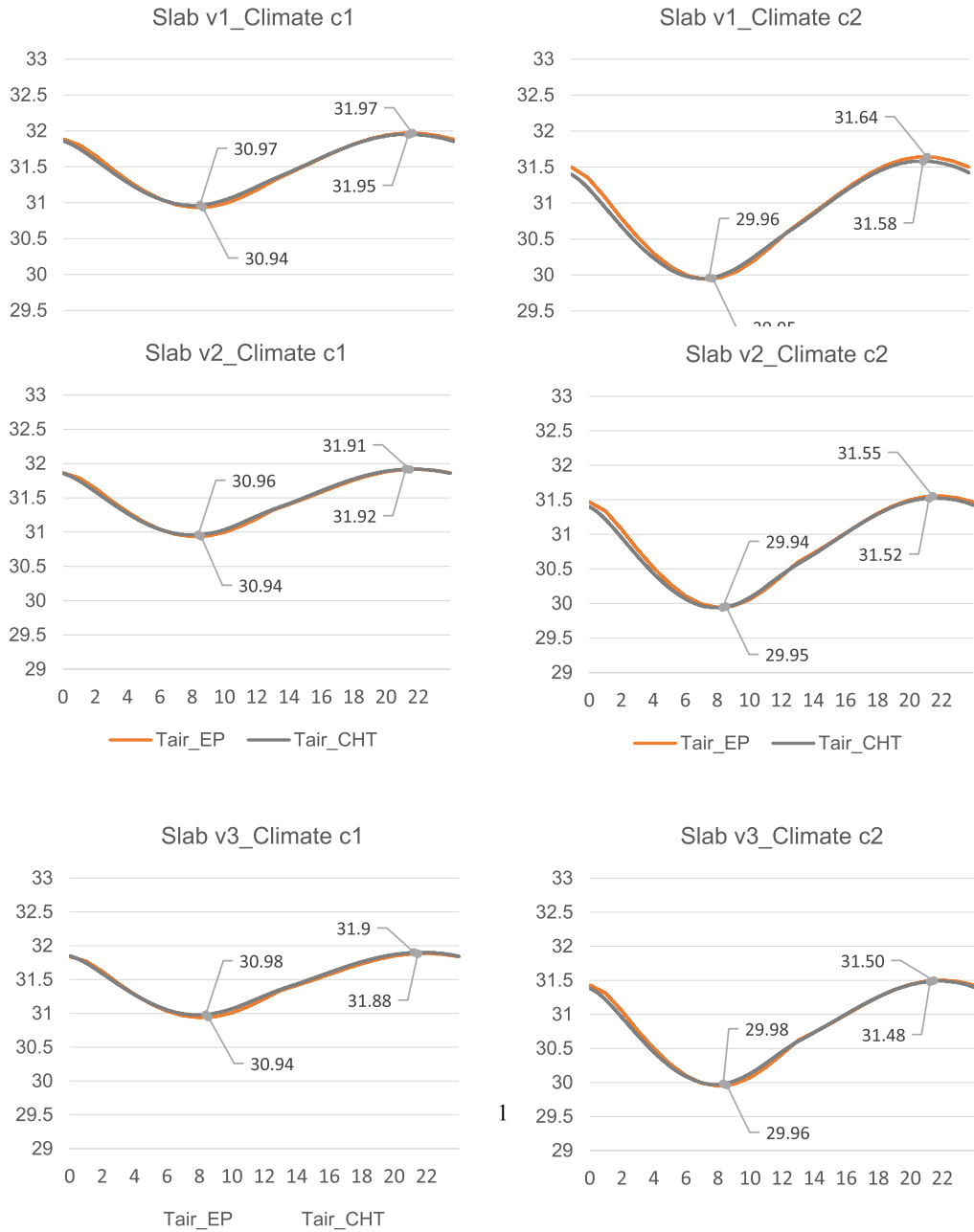
Fig. A.1a-A.1j. Results comparison between CHT and EnergyPlus (EP) simulations for identical sinusoidal boundary conditions
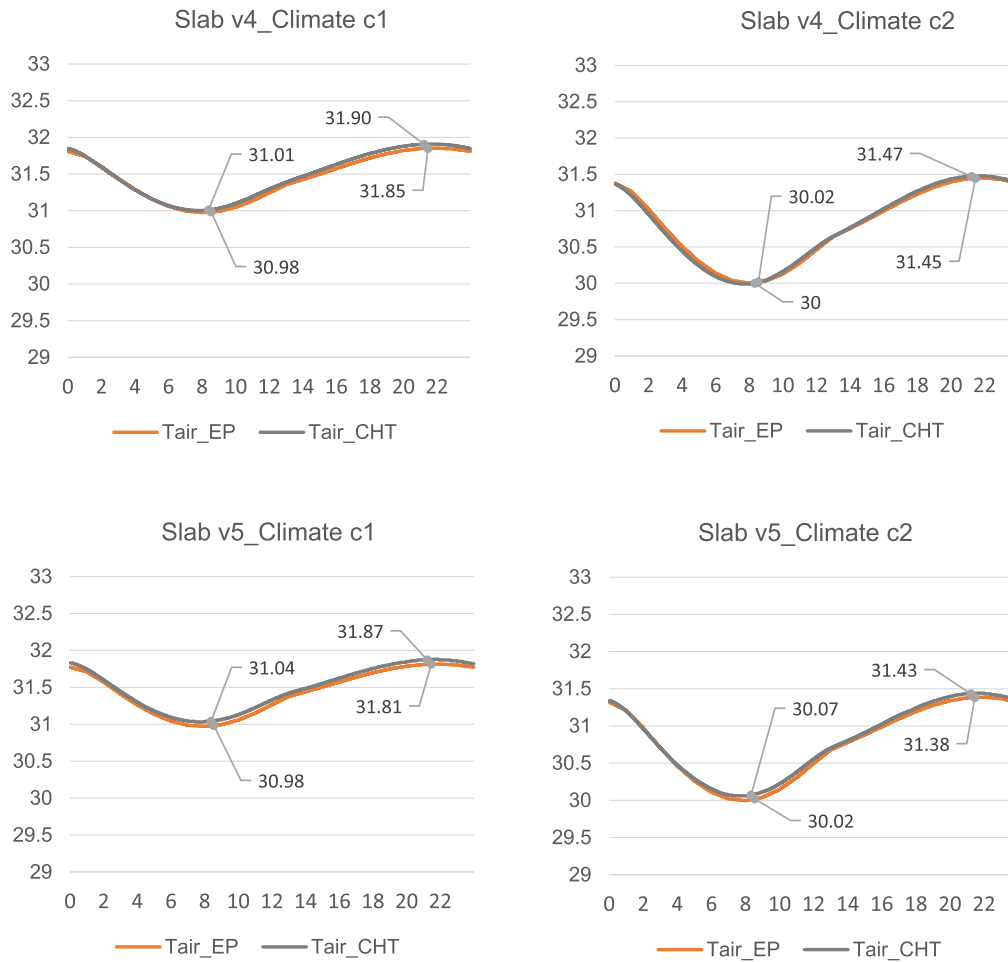
Fig. A.1a–A.1j. (*continued*).

As shown in the above figures A1a-A1j, both simulations show a strong agreement both in the time lag and attenuation of the computed indoor temperature fluctuations. More importantly, EnergyPlus succeeds in capturing the trend found in previous work conducted by the authors [3]: despite the reduction on structural mass (the concrete volume in v1 is 30% less than v5), the thermal mass performance remains unaltered, slightly improving in all cases thanks to the enhanced convective heat transfer rate. This performance is also shown in Figure A2, which highlights the dynamic performance of all six slab geometries throughout two 24-h cycles. As mentioned in section 4.2, the damping coefficient is increased between 6% and 9% for all five shaped geometries, relative to the flat 12 cm concrete slab. The methods and metrics used to capture this dynamic performance are further explained in Ref. [3].
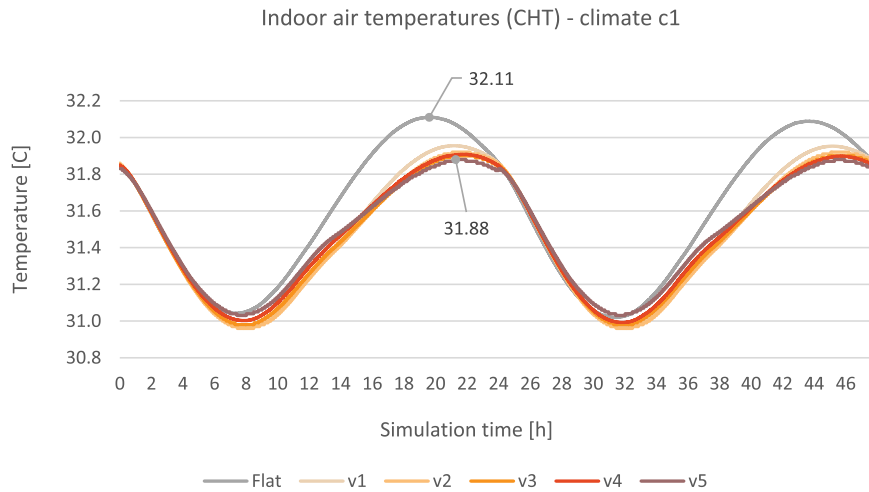
Fig. A.2. Indoor air temperatures obtained from a 48h CHT simulation for all six slab geometries.

Appendix B

The simulations settings used in section 3.2 were validated using two experimental data that have been commonly used as validation data in previous research work on room airflow analysis [42]. First, the natural convection conditions are compared with the results from Olson et al. [43]. The test chamber consists of a closed room of 7.9 × 2.5 × 1.5 m with a cold and hot wall to each side. Temperatures obtained were measured in the central plane X = 3.95. Figure B1 illustrates how the RNG k-ɛ model [46] matches the temperature profile obtained from the experimental data.
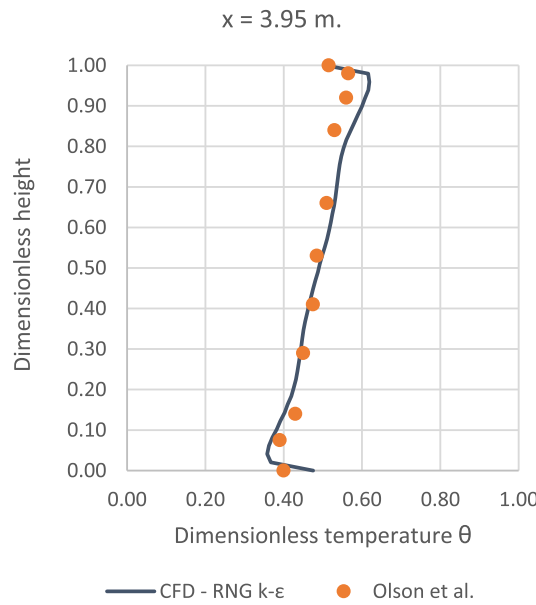
Fig. B.1. Experimental and simulation results for natural convection case at central plane X = 3.95

The dimensionless temperature is computed using the following relation, where T_c is the constant temperature of the cold surfaced and T_h the temperature of the hot surface.

$$\theta = \frac{T - T_c}{T_h - T_c} \tag{B.1}$$

Moreover, Figure B2 shows how the simulation also succeeded in predicting the recirculation pattern observed in the original experiment.
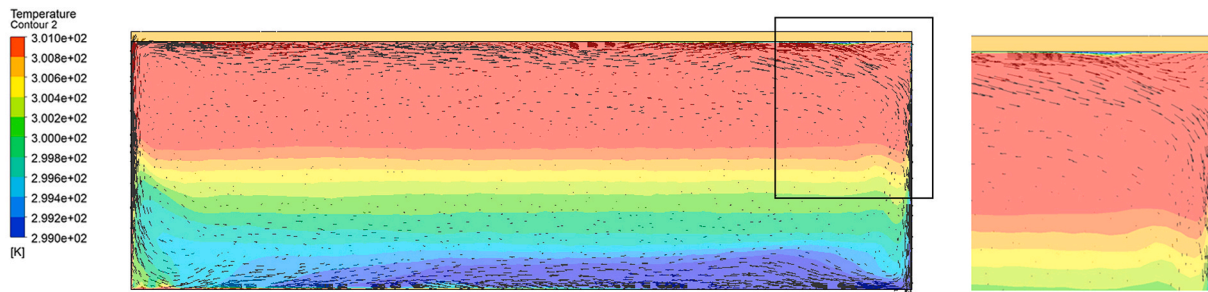
Fig. B.2. temperature profile and velocity vectors across the simulated room with the hot and cold surfaces at 35.3C and 19.9C respectively. Right: the velocity vectors reveals how the simulation succeeds in predicting the recirculation pattern overserved in the experiments from Olson et al.

Furthermore, the experiment conducted by Blay et al. [44] was used to validate mixed convection conditions that, although not present in this work, could be implemented in future research. In this case, the test chamber is defined by a $1.04 \times 1.04 \times 0.7$ room with a supply air at 15.0C and a heated floor at 35.5C. Figure B3 and figure B4 illustrate how our simulations present a good agreement with the experimental data. Figure B5 shows the experimentally anticipated clockwise flow that is created thanks to high jet momentum in relation to the buoyancy forces caused by the heated floor.
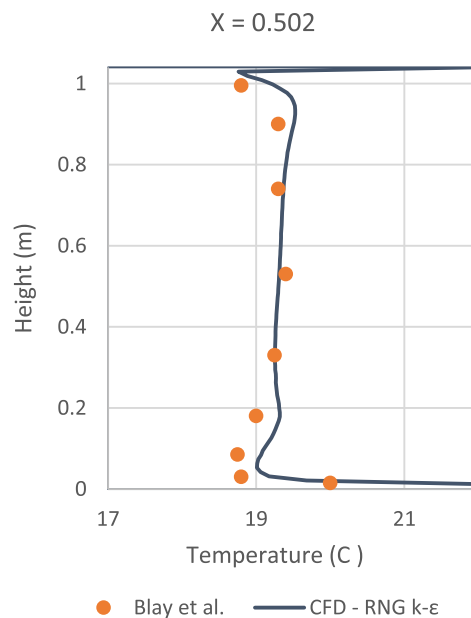
Fig. B.3. Experimental and simulation results for mixed convection case at central plane X = 0.52

Z = 0.502
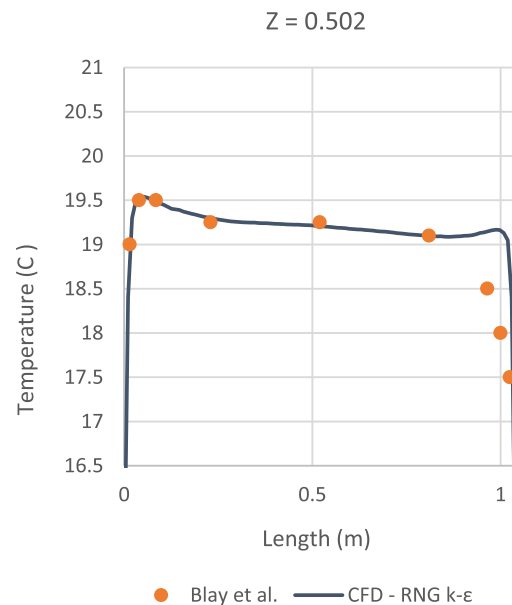
Fig. B.4. Experimental and simulation results for mixed convection case at central plane Z = 0.52
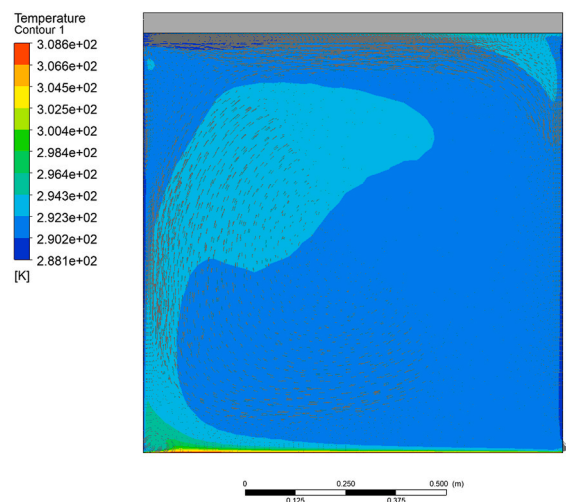
Fig. B.5. temperature profile and velocity vectors across the simulated room. Left top: inlet at 15C and 0.57 m/s. Bottom-right: pressure outlet

References

[1] S.N. Islam, J. Winkel, Climate change and social inequality. https://www.un.org/development/desa/publications/working-paper/wp152, 2017, 32.

[2] J.M. Allwood, M.F. Ashby, T.G. Gutowski, E. Worrell, Material efficiency: a white paper, Resources, Conserv. Recycl. 55 (2011) 362–381, https://doi.org/10.1016/j.resconrec.2010.11.002.

[3] E. Gascón Alvarez, C.T. Mueller, L.K. Norford, Dynamic thermal performance of structurally optimized concrete floor slabs, in: Proceedings of the 17th International IBPSA Conference, 2021. Bruges (Belgium).

[4] Technology Roadmap, Low-carbon transition in the cement industry. https://www.iea.org/reports/technology-roadmap-low-carbon-transition-in-the-cement-industry.

[5] B. Lebot, Global status report 2017. https://www.worldgbc.org/news-media/global-status-report-2017.

[6] N. Huberman, D. Pearlmutter, E. Gal, I.A. Meir, Optimizing structural roof form for life-cycle energy efficiency. https://doi.org/10.1016/j.enbuild.2015.07.008, 2015, 336-349.

[7] A. Liew, D.L. López, T. Van Mele, P. Block, Design, fabrication and testing of a prototype, thin-vaulted, unreinforced concrete floor, Eng. Struct. 137 (2017) 323–335, https://doi.org/10.1016/j.engstruct.2017.01.075.

[8] W. Hawkins, J. Orr, P. Shepherd, T. Ibell, J. Bregulla, Thin-shell textile-reinforced concrete floors for sustainable buildings, in: Proceedings of IASS Annual Symposia, 2017. Hamburg (Germany).

[9] M.A. Ismail, C.T. Mueller, Minimizing embodied energy of reinforced concrete floor systems in developing countries through shape optimization, Eng. Struct. 246 (2021), 112955, https://doi.org/10.1016/j.engstruct.2021.112955.

[10] D. Aviv, K.W. Chen, E. Teitelbaum, D. Sheppard, J. Pantelic, A. Rysanek, F. Meggers, A fresh (air) look at ventilation for COVID-19: estimating the global energy savings potential of coupling natural ventilation with novel radiant cooling strategies, Appl. Energy 292 (2021), 116848, https://doi.org/10.1016/j.apenergy.2021.116848.

[11] J. Grinham, S. Craig, D.E. Ingber, M. Bechthold, Origami microfluidics for radiant cooling with small temperature differences in buildings, Appl. Energy 277 (2020), 115610, https://doi.org/10.1016/j.apenergy.2020.115610.

[12] M. Ye, A.A. Serageldin, A. Radwan, H. Sato, K. Nagano, Thermal performance of ceiling radiant cooling panel with a segmented and concave surface: laboratory analysis, Appl. Therm. Eng. 196 (2021), 117280, https://doi.org/10.1016/j.applthermaleng.2021.117280.

[13] L. Zhang, X.-H. Liu, Y. Jiang, Experimental evaluation of a suspended metal ceiling radiant panel with inclined fins, Energy Build. 62 (2013) 522–529, https://doi.org/10.1016/j.enbuild.2013.03.044.

[14] S. Craig, The optimal tuning, within carbon limits, of thermal mass in naturally ventilated buildings, Build. Environ. 165 (2019), 106373, https://doi.org/10.1016/j.buildenv.2019.106373.

[15] R. Fortin, S. Craig, Geometrically activated thermal mass: wood vs. concrete, J. Phys.: Conf. Ser. 2042 (2021), 012156, https://doi.org/10.1088/1742-6596/2042/1/012156.

[16] T. Kim, S. Kato, S. Murakami, Indoor cooling/heating load analysis based on coupled simulation of convection, radiation and HVAC control, Build. Environ. 36 (2001) 901–908, https://doi.org/10.1016/S0360-1323(01)00016-6.

[17] N. Fonseca, S. Bertagnolio, C. Cuevas, Radiant ceiling systems coupled to its environment part 2: dynamic modeling and validation, Appl. Therm. Eng. 30 (2010) 2196–2203, https://doi.org/10.1016/j.applthermaleng.2010.05.032.

[18] J. Liu, M. Heidarinejad, S. Gracik, J. Srebric, The impact of exterior surface convective heat transfer coefficients on the building energy consumption in urban neighborhoods with different plan area densities, Energy Build. 86 (2015) 449–463, https://doi.org/10.1016/j.enbuild.2014.10.062.

[19] H. Afshari, W. Hare, S. Tesfamariam, Constrained multi-objective optimization algorithms: review and comparison with application in reinforced concrete structures, Appl. Soft Comput. 83 (2019), 105631, https://doi.org/10.1016/j.asoc.2019.105631.

[20] N.C. Brown, V. Jusiega, C.T. Mueller, Implementing data-driven parametric building design with a flexible toolbox, Autom. ConStruct. 118 (2020), 103252 https://doi.org/10/gg55cf.

[21] K. Deb, A. Pratap, S. Agarwal, T. Meyarivan, A fast and elitist multiobjective genetic algorithm: nsga-II, IEEE Trans. Evol. Comput. 6 (2002) 182–197, https://doi.org/10.1109/4235.996017.

[22] M. Sadeghipour Roudsari, M. Pak, Ladybug: a parametric environmental plugin for grasshopper to help designers create an environmentally-conscious design, in: Proceedings of the 13th International IBPSA Conference, 2013. Lyon, France.

[23] M.A. Menchaca-Brandan, F.A. Dominguez Espinosa, L.R. Glicksman, The influence of radiation heat transfer on the prediction of air flows in rooms under natural ventilation, Energy Build. 138 (2017) 530–538, https://doi.org/10.1016/j.enbuild.2016.12.037.

[24] Z. Zhang, W. Zhang, Z.J. Zhai, Q.Y. Chen, Evaluation of various turbulence models in predicting airflow and turbulence in enclosed environments by CFD: Part 2—comparison with experimental data from literature, HVAC R Res. 13 (2007) 871–886, https://doi.org/10.1080/10789669.2007.10391460.

[25] EN ISO 11855-2:2021, Building Environment Design - Embedded Radiant Heating and Cooling Systems - Part 2: Determination of the Design of Heating and Cooling Capacity, 2021.

[26] K.A. Antonopoulos, M. Vrachopoulos, C. Tzivanidis, Experimental and theoretical studies of space cooling using ceiling-embedded piping, Appl. Therm. Eng. 17 (1997) 351–367.

[27] J. Kośny, E. Kossecka, Multi-dimensional heat transfer through complex building envelope assemblies in hourly energy simulation programs, Energy Build. 34 (2002) 445–454, https://doi.org/10.1016/S0378-7788(01)00122-0.

[28] J. Liu, M. Heidarinejad, S. Gracik, J. Srebric, The impact of exterior surface convective heat transfer coefficients on the building energy consumption in urban neighborhoods with different plan area densities, Energy Build. 86 (2015) 449–463, https://doi.org/10.1016/j.enbuild.2014.10.062.

[29] I. Beausoleil-Morrison, The adaptive simulation of convective heat transfer at internal building surfaces, Build. Environ. 37 (2002) 791–806, https://doi.org/10.1016/S0360-1323(02)00042-2.

[30] R. Karadağ, New approach relevant to total heat transfer coefficient including the effect of radiation and convection at the ceiling in a cooled ceiling room, Appl. Therm. Eng. 29 (2009) 1561–1565, https://doi.org/10.1016/j.applthermaleng.2008.07.005.

[31] F. Alamdari, G.P. Hammond, Improved data correlations for buoyancy-driven convection in rooms, Build. Serv. Eng. Technol. 4 (1983) 106–112, https://doi.org/10.1177/014362448300400304.

[32] Y. Yuan, X. Zhang, X. Zhou, Simplified correlations for heat transfer coefficient and heat flux density of radiant ceiling panels, Science and Technology for the Built Environment 23 (2017) 251–263, https://doi.org/10.1080/23744731.2016.1203714.

[33] J. Shinoda, O.B. Kazanci, S. Tanabe, B.W. Olesen, A review of the surface heat transfer coefficients of radiant heating and cooling systems, Build. Environ. 159 (2019), 106156, https://doi.org/10.1016/j.buildenv.2019.05.034.

[34] S. Carlisle, B. Waldman, M. Lewis, K. Simonen, Carbon Leadership Forum Material Baseline Report (Version 2), Carbon Leadership Forum, University of Washington, 2021. http://hdl.handle.net/1773/47141, 2021.

[35] M. Qu, O. Abdelaziz, Z. Gao, H. Yin, Isothermal membrane-based air dehumidification: a comprehensive review, Renew. Sustain. Energy Rev. 82 (2018) 4060–4069, https://doi.org/10.1016/j.rser.2017.10.067.

[36] BP statistical review of world energy 2020. https://www.bp.com/en/global/corporate/energy-economics/statistical-review-of-world-energy.html.

[37] S. Nicholson, G. Heath, Life cycle greenhouse gas emissions from electricity generation: update. https://www.nrel.gov/analysis/life-cycle-assessment.html, 2021.

[38] EC3, Product brief. https://www.buildingtransparency.org/resources/ec3-downloads/.

[39] Y. Wu, H. Sun, M. Duan, B. Lin, H. Zhao, Dehumidification-adjustable cooling of radiant cooling terminals based on a flat heat pipe, Build. Environ. 194 (2021), 107716, https://doi.org/10.1016/j.buildenv.2021.107716.

[40] Y. Liang, N. Zhang, H. Wu, X. Xu, K. Du, J. Yang, Q. Sun, K. Dong, G. Huang, Thermal environment and thermal comfort built by decoupled radiant cooling units with low radiant cooling temperature, Build. Environ. 206 (2021), 108342, https://doi.org/10.1016/j.buildenv.2021.108342.

[41] R.K. Strand, K.T. Baumgartner, Modeling radiant heating and cooling systems: integration with a whole-building simulation program, Energy Build. 37 (2005) 389–397, https://doi.org/10.1016/j.enbuild.2004.07.009.

[42] Liangjun Zhang, Yiye Huang, Guang Yang, Jingyi Wu, Numerical simulation of conjugate turbulent mixed convection in an open cavity: evaluation of different wall heat conduction models, Numer. Heat Tran., Part A: Applications 74 (5) (2018) 1244–1264.

[43] D.A. Olson, L.R. Glicksman, H.M. Ferm, Steady-state natural convection in empty and partitioned enclosures at high Rayleigh numbers, J. Heat Tran. 112 (1990) 640–647, https://doi.org/10.1115/1.2910435.

[44] D.S. Mergui Blay, C. Niculae, Confined turbulent mixed convection in the presence of horizontal buoyant wall jet, Fundamentals of Mixed Convection 213 (1992) (1992) 65–72.

[45] Ladybug tools for grasshopper documentation. https://docs.ladybug.tools/ladybug-primer/components/3_analyzegeometry/view_percent.

[46] Q. Chen, Comparison of different k-ε models for indoor air flow computations, Numer. Heat Tran., Part B: Fundamentals. 28 (1995) 353–369, https://doi.org/10.1080/10407799508928838.

[47] J.H.L. IV, D.J.H.L. V, A Heat Transfer Textbook, fifth ed., Dover Publications, Mineola, New York, 2019. Reprint edition.